Monthly Notices of the ROYAL ASTRONOMICAL SOCIETY

MNRAS **549,** 1–20 (2026)
Advance Access publication 2026 April 28

https://doi.org/10.1093/mnras/stag781

GOALS-*JWST*: resolved multiphase molecular gas in IRAS 20551-4250 using *JWST* and ALMA

D. Kakkad [1,2★] Y. Song,[3,4] T. S.-Y. Lai,[5] L. Armus,[5] M. Malkan,[6] K. L. Larson [7] A. S. Evans,[8,9] P. N. Appleton,[10] L. Barcos-Muñoz,[8,9] M. Bianchin [11,12,13] T. Böker [14] T. Bohn,[15] V. Buiten,[16] V. Charmandaris,[17,18,19] T. Diaz-Santos,[17,18] H. Inami [20] J. Kader,[11] L. Lenkic,[5] S. T. Linden,[21] C. M. Lofaro,[18,22] G. C. Privon [8,9,23] C. Ricci,[24,25] M. Sanchez-Garcia,[18] D. Sanders,[26] N. Torres-Alba,[27] V. U[5,11] and P. van der Werf[16]

Affiliations are listed at the end of the paper

Accepted 2026 April 20. Received 2026 April 20; in original form 2025 October 27

ABSTRACT

Studying the content and distribution of molecular gas (H_2) provides key insights into how feedback from active galactic nuclei (AGNs) and star formation influences galaxy evolution, since molecular gas is the primary fuel for star formation. Ultra-luminous infrared galaxies (ULIRGs) are ideal candidates to study how AGNs and/or starbursts affect the interstellar medium due to their intense AGN and star-forming activity. We present spatially resolved multiphase molecular gas study of IRAS20551-4250, a nearby ($z = 0.0429$) ULIRG, using *James Webb Space Telescope* (*JWST*)/MIRI-MRS and ALMA. Mid-infrared diagnostics do not rule out the presence of AGNs in IRAS20551-4250. [O III]λ5007 in VLT/MUSE data reveal ionized gas outflows with $w_{80}^{[OIII]} \sim 790$ km s^{-1} and $\dot{M}_{out}^{[OIII]} < 0.01$ M$_\odot$ yr^{-1}. No outflows are observed in either molecular phases. *JWST*/MIRI-MRS data reveal several rotational transitions of warm H_2 ($T\sim$ 500–1400 K) within the central $\sim 4 \times 4$ kpc^2 region. Excitation temperature maps suggest that the warm H_2 is primarily heated by UV radiation from the central source. The CO-based cold molecular component dominates the molecular gas mass, accounting for >95 per cent of the total molecular gas mass. Warm H_2 maps show two tidal tails and the velocity centroid maps show disturbed non-rotational motions and a systematic gradient across the field of view, similar to that of ALMA CO-based cold molecular gas and consistent with a late-stage merger. Together, our analysis indicate that the molecular gas composition in IRAS20551-4250 is consistent with ongoing star formation in the host galaxy and the outflows observed in ionized gas phase appear insufficient to expel the molecular gas or quench ongoing star formation.

Key words: galaxies: active – galaxies: evolution – galaxies: starburst – techniques: spectroscopic – infrared: galaxies.

1 INTRODUCTION

Feedback from star formation and accreting supermassive black holes, also called active galactic nuclei (AGNs) feedback, have become primary ingredients of all simulations that model galaxy formation and evolution (e.g. J. Schaye et al. 2015, 2023; P. F. Hopkins et al. 2018; A. Pillepich et al. 2018; M. Vogelsberger et al. 2020). Over the past decade, several observations have now confirmed the presence of high-velocity outflows (outflow velocity, v_{out} >1000 km s^{-1}) in low-redshift and high-redshift AGNs and star-forming galaxies in multiple gas phases, namely neutral, ionized, and molecular (e.g. D. S. N. Rupke & S. Veilleux 2011; C. Cicone et al. 2014; R. Genzel et al. 2014; C. M. Harrison et al. 2014; R. Davies et al. 2020, 2024; D. Kakkad et al. 2020, 2022; A. Vayner et al. 2024; A. Weldon et al. 2024). These outflows are believed to have the potential to sweep the host galaxies clean of molecular gas and eventually quench star formation (e.g. J. M. Piotrowska et al. 2022).

Several efforts on the observational front are underway to understand how these outflows affect the host galaxy properties such as the star formation rate (SFR) using spatially resolved spectroscopy (e.g. G. Cresci et al. 2015b; S. Carniani et al. 2016; R. Maiolino et al. 2017; J. Scholtz et al. 2020; P. S. Bessiere & C. Ramos Almeida 2022; D. Kakkad et al. 2023; K. M. Dasyra et al. 2024). However, connecting the AGN activity (AGN luminosity or outflow power) with the host's ongoing SFR has not been straightforward, because of the difference in the time-scales of the AGN activity, outflow propagation, and star formation (e.g. R. C. Kennicutt & N. J. Evans 2012; K. Schawinski et al. 2015). Furthermore, the heterogenous geometry of the galaxies, orientation effects, and different AGN types (type-1 and type-2) further make the calculation of the outflow quantities challenging (A. Castro et al. 2025). In addition to AGN feedback, feedback

★ E-mail: darshankakkad@gmail.com

© The Author(s) 2026.
Published by Oxford University Press on behalf of Royal Astronomical Society. This is an Open Access article distributed under the terms of the Creative Commons Attribution License (https://creativecommons.org/licenses/by/4.0/), which permits unrestricted reuse, distribution, and reproduction in any medium, provided the original work is properly cited.

Downloaded from https://academic.oup.com/mnras/article/549/1/stag781/8664325 by Instituto de Astrofisica de Canarias user on 26 June 2026

from starburst or supernovae may also play a crucial role in driving turbulence (e.g. S. Koudmani, D. Sijacki & M. C. Smith 2022).

A direct method to test the impact of AGN or star formation feedback on host galaxies is by observing the molecular gas itself. The total content of molecular gas may be treated as a reliable indicator of the star-forming capacity of galaxies (see reviews by R. C. Kennicutt & N. J. Evans 2012; C. L. Carilli & F. Walter 2013; S. Veilleux et al. 2020; A. Saintonge & B. Catinella 2022). In the presence of an outflow, it is the gas phase that will be affected first before any impact on star formation is observed. Therefore, any impact on star formation should first be visible as an impact on the overall molecular gas content and/or composition. Molecular gas itself comes in multiple phases and can be broadly divided into three categories depending on the gas temperature. The cold phase (T<100 K) is usually traced using transitions in sub-mm spectra (e.g. CO, HCN), the warm molecular gas phase (T = few hundred K) is traced via rotational transitions of the hydrogen molecule in the mid-infrared spectra, and the hot phase (1000 K< T< 3000 K) is traced via ro-vibrational transitions of the hydrogen molecule in the near-infrared spectra (e.g. P. Maloney & J. H. Black 1988; M. G. Burton, D. J. Hollenbach & A. G. G. Tielens 1992; D. Kakkad et al. 2025).

The majority of molecular gas studies in the literature over the previous decade have focused on the cold gas phase using different transitions of CO. Comparative study of cold molecular gas in mass-matched samples of AGNs and star-forming galaxies at low- and high-redshift have yielded conflicting results, with some showing low molecular gas content in AGNs and others showing AGNs live in the same or gas-rich environment as star-forming galaxies (see B. Husemann et al. 2017; D. Kakkad et al. 2017; D. J. Rosario et al. 2018; C. Circosta et al. 2021; M. J. Koss et al. 2021; E. Bertola et al. 2024). These differences may be due to different CO excitation corrections or CO-to-H_2 conversion factor (α_{CO}) between AGNs and non-AGN galaxies. Another proposed explanation is that the impact on molecular gas should be more evident in regions closer to the black hole, where a higher abundance of warm and hot H_2 gas is expected (see V. U et al. 2019).

Indeed, there has been a parallel effort to get a more detailed spatially resolved view of the molecular gas properties from sub-pc to a few hundred parsec scales, by mapping multiphase molecular gas in near-infrared, mid-infrared, and sub-mm wavelengths using integral field spectroscopy (IFS). For instance, S. García-Burillo et al. (2021) reported signs of nuclear scale CO-based molecular gas deficits in a sample of low-redshift luminous Seyfert host galaxies, with extreme gas deficits observed in galaxies that host molecular outflows as well. D. J. Rosario et al. (2019) also reported an abundance of ro-vibrational transition, H_2 2.12 μm tracing hot molecular gas, in regions lacking CO-based cold molecular gas (see also C. Feruglio et al. 2020; R. Davies et al. 2024; D. Esparza-Arredondo et al. 2025). The emerging picture from these individual multiphase molecular gas studies is that although the outflows may not remove molecular gas from the host galaxies, they may heat the gas in the circum-nuclear regions via shocks or X-ray radiation.

In this regard, luminous infrared galaxies (LIRGs) and ultraluminous infrared galaxies (ULIRGs) are particularly interesting targets to study the impact of feedback from starbursts and/or AGNs on the hosts' molecular gas. ULIRGs are often a result of mergers and the exchange of gas during the merger results in an intense starburst and, at the same time, fuel gas and dust on to the central supermassive black hole. The primary radiation field in ULIRGs is often reprocessed by dust, which results in very high infrared luminosities. The intense radiation, combined with a gas-rich environment, means ULIRGs are prime sites for hosting fast outflows (e.g. M. Pereira-Santaella et al. 2018; I. Lamperti et al. 2022). As a result, shocked molecular gas or molecular gas heated by X-rays is expected to be common in these galaxies (see H. Sugai et al. 1997; V. U et al. 2019).

In this paper, we present multiphase gas properties of a nearby ULIRG, IRAS 20551–4250 (also named ESO 286–19 or ESO 286-IG019, RA = 20:58:26.82, Dec. = −42:38:59.41, z = 0.0429). Hereafter, we simply refer to this system as IR20551. IR20551 is a part of the Great Observatories All-sky LIRG Survey (GOALS; see L. Armus et al. 2009). The GOALS survey consists of a sample of bright (S_{60} > 5.24 Jy) LIRGs, selected from the IRAS revised bright galaxy sample (see D. B. Sanders et al. 2003). IR20551 was first discovered within the photometric and spectroscopic ESO/Uppsala programme, as reported in R. M. West et al. (1978). Its exceptionally bright infrared nature was confirmed in L. Johansson (1991), which was attributed to warm dust heated by young stars. Subsequently, IR20551 has been targeted by several multiwavelength campaigns to unveil the true nature of the host galaxy and its nucleus (e.g. R. Genzel et al. 1998; K. Misaki et al. 1999; A. Franceschini et al. 2003; D. Farrah et al. 2007; S. Haan et al. 2011; E. Sani & E. Nardini 2012; S. Stierwalt et al. 2013, 2014; M. Imanishi, K. Nakanishi & T. Izumi 2016). These multiwavelength observations have suggested that IR20551 is an interacting system in a fairly advanced stage of merger with a disturbed core and a prominent tidal tail (Fig. 1). It is very bright in the infrared with $L_{IR} = 1.15 \times 10^{12}$ $L_\odot$ (L. Armus et al. 2009), placing the target in the ULIRG category.

IR20551 is a composite system, which shows possible signatures of both AGN activity and a starburst, depending on the waveband of observation. For example, at optical wavelengths, this target is classified as an H II region (L. Johansson 1991) and mid-infrared observations indicate both starburst and possible AGN contribution (e.g. R. Genzel et al. 1998). The AGN nature of IR20551 is also indicated based on its hard X-ray luminosity, $\log L_{X(2-10\ keV)} = 42.8$ erg s^{-1} (close to the threshold of AGN classification $\log L_{X(2-10\ keV)} > 42.5$ erg s^{-1} P. Padovani et al. 2017; R. C. Hickox & D. M. Alexander 2018; M. L. Saade et al. 2022), and an X-ray column density, $N_H = 8 \times 10^{23}$ cm^{-2} (e.g. A. Franceschini et al. 2003). A recent joint NuSTAR+XMM+ *Chandra* analysis of this source did not rule out the presence of an obscured AGN in this source (see S. Yamada et al. 2021). The implied X-ray column density suggests that the AGN, if confirmed, is heavily obscured. A quantitative estimate for the contribution of the AGN to infrared emission was reported by D. Farrah et al. (2007), who suggest that due to the heavy obscuration, typical AGN tracers such as [Ne V] and [O IV] (L. Spinoglio, J. A. Fernández-Ontiveros & M. A. Malkan 2022) are absent in its mid-IR spectra. Atacama Large Millimetre-submm Array (ALMA) observations of IR20551 over the last decade have also confirmed the presence of dense molecular gas, as traced by species such as HCN or HCO+, suggesting an abundant molecular gas supply able to sustain star formation or feed AGN in the centre (e.g. M. Imanishi et al. 2016).

In this paper, we present detailed multiwavelength imaging and IFS observations of IR20551. Specifically, we will present the mid-infrared spectral properties using the Medium Resolution Spectrograph (MRS) of the Mid-InfraRed Intrument (MIRI)

Downloaded from https://academic.oup.com/mnras/article/549/1/stag781/8664325 by Instituto de Astrofisica de Canarias user on 26 June 2026

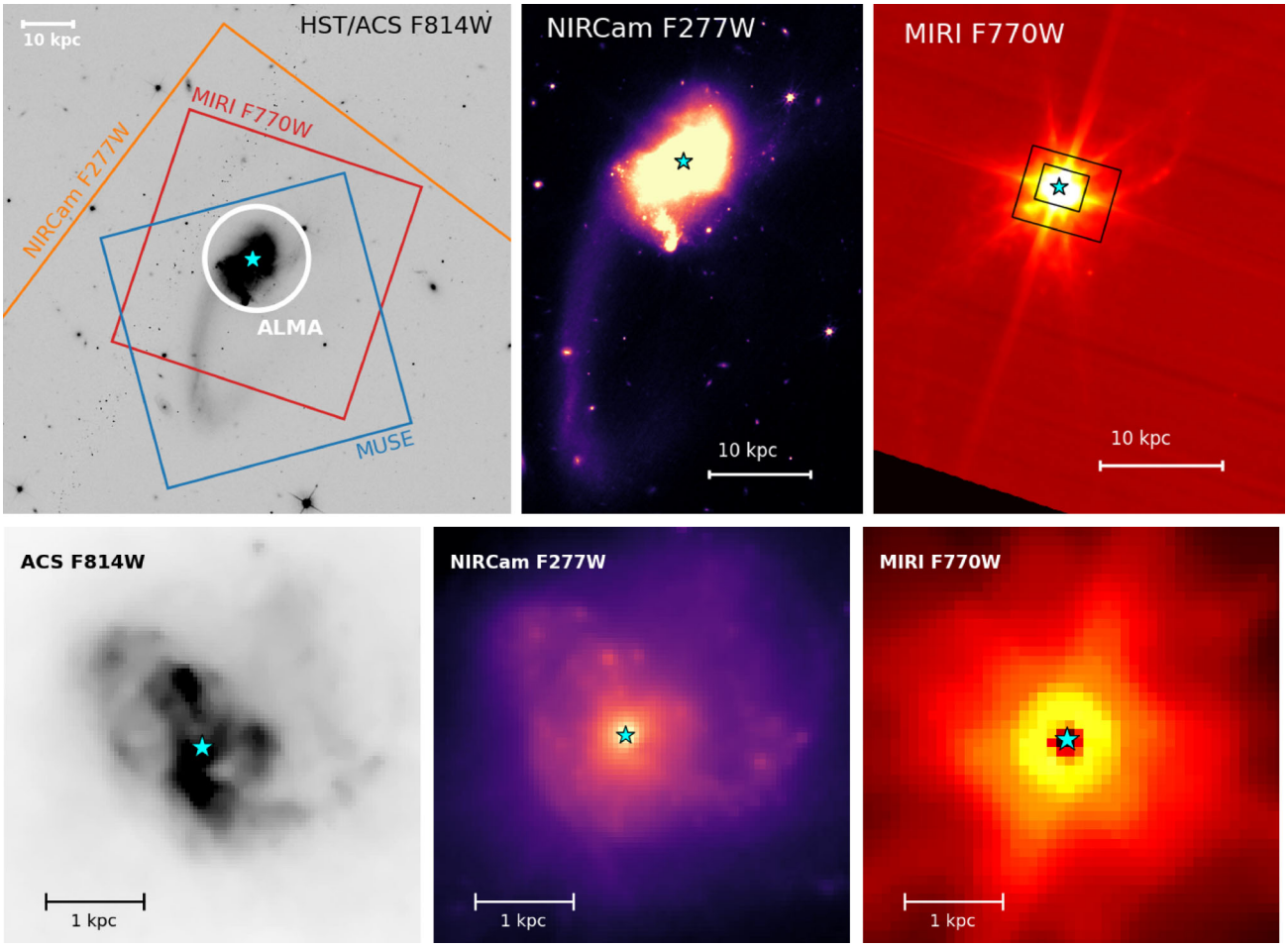


Figure 1. The top panels show images from *HST*/ACS *F*814*W* (top left), *JWST*/NIRCam *F*277*W* (top middle), and *JWST*/MIRI *F*770*W* (top right) covering the full range of spatial scales of IR20551. The horizontal bar in all the top panels show the 10 kpc physical scale. The overlaid white circle, red rectangle, orange rectangle, and blue rectangle in the top left image shows the ALMA, MIRI, NIRCam, and MUSE coverage regions. The black rectangle in the top right panel shows the regions covered by Channels 1 and 4 of the MRS. The bottom panels show the same sequence as the top panels, but zoomed in the central 5×5 arcsec^2 region of the galaxy. The *HST* and NIRCam images clearly show the presence of extended tidal tail towards the SE direction from the galaxy centre. The MIRI image shows a faint SE tail, but a prominent NW tail, not clearly visible in the *HST* and NIRCam images. The *HST* image does not show a clear point source in the centre, but shows clumpy morphology within the central region, while the NIRCam and MIRI images show a very bright point source at the centre. In fact, the central region in the MIRI image is saturated due to emission from a putative AGN. The horizontal bar shows the 1 kpc physical scale in the bottom panels. The cyan star marks the location of the putative AGN. North is up and East is left in all panels.

aboard *James Webb Space Telescope* (*JWST*) and CO(2-1) spectra using ALMA. We compliment these data with archival Multi-Unit Spectroscopic Explorer (MUSE) data at the Very Large Telescope (VLT) and the Advanced Camera for Surveys (ACS) aboard *Hubble Space Telescope* (*HST*). The aims of this paper are to investigate the true nature of the nuclear regions in this galaxy, characterize cold and warm molecular gas properties, and infer if the molecular gas observations provide any evidence of feedback from starburst or AGN, as is often expected in ULIRGs. This paper is organized as follows: In Section 2, we present the details of the observing data sets used from *JWST*, ALMA, and the VLT. Following this, in Section 3, we present our analysis methods for each data set and the results alongside them and in Sections 4 and 5, we discuss the implications of these results and the conclusions of this work, respectively. Throughout this paper, we use the following cosmology: $H_0 = 70$ km s^{-1}, $\Omega_M = 0.3$, and $\Omega_\Lambda = 0.7$. Unless mentioned otherwise, North is up and East is to left in all the maps presented in this paper.

2 OBSERVATIONS AND DATA REDUCTION

In this section, we describe the observations and data reduction of the multiwavelength data presented in this paper.

2.1 *JWST*/MIRI-MRS

IR20551 was observed on 2023 October 16 using MRS (M. Wells et al. 2015), as a part of the Cycle-2 General Observer (GO) programme PID3368 (co-PIs: Armus & Evans). No target acquisition was performed, as the pointing accuracy of 0.1 arcsec was sufficient to centre the target in the MRS field of view. The observation consisted of a single IFU pointing, centred on the infrared-bright nucleus. We used a 4-point dither pattern, which improved the spatial sampling and resolution of the final drizzled data cube (see D. R. Law et al. 2023). Separate background exposures were taken along with the on-source observations as a non-interruptible sequence to subtract the infrared background emission, especially in Channels 3 and 4. During the background

Downloaded from https://academic.oup.com/mnras/article/549/1/stag781/8664325 by Instituto de Astrofisica de Canarias user on 26 June 2026

observations, simultaneous MIRI imaging of the target was performed in filters *F560W*, *F777W*, and *F1500W*. Given the very bright nucleus, the BRIGHTSKY subarray was used to avoid saturation.

The MRS observations covered all four channels and their sub-bands (SHORT, MEDIUM, and LONG), resulting in a contiguous wavelength coverage between 4.9 and 27.9 μm (∼4.7–26.7 μm in the rest frame) with a resolving power ∼1300–3700 (highest resolving power in the short-wavelength channels). The field of view varies between $\sim 3.2 \times 3.7$ and 6.6×7.7 arcsec^2 and PSF between 0.25 and 1.0 arcsec from Channels 1–4. The observations employed a FASTR1 readout mode for a single exposure with 80 groups per integration and one integration per exposure. The total exposure time was 888 s per channel.

We used the standard MRS data reduction procedure using the *JWST* pipeline (version: 1.15.1, see A. Labiano et al. 2016) using the Calibration Reference Data System context `jwst_1256.pmap`. Wherever necessary, we also employed additional customized steps and fine-tuned pipeline parameters during the data reduction to improve data quality, which are briefly summarized here. There are three stages to the MRS data reduction pipeline: The first stage performs detector-level corrections, where we turned on the `find_showers` keyword and kept the rest of the default pipeline parameters unchanged. The `find_showers` keyword helps identify and correct for cosmic ray showers. Some warm pixels still remain unidentified in this stage. To remove these, we derived the median of all slope images (`*rate.fits` files) obtained in the output of stage-1 and applied a standard sigma-clipping algorithm to flag the outliers as `DO_NOT_USE` in the bad pixel mask.

The files with the updated bad pixel masks were then processed during the second stage of the pipeline, which performs instrument calibrations such as flux and wavelength calibration and flat-field correction. This stage also performs additional corrections to residual fringes in the individual channels by setting the parameter `skip_residual_fringe` to `FALSE`. The background subtraction was performed using the dedicated background exposures. The output of this second stage of the pipeline is a set of fully calibrated individual exposures (`*cal.fits` files).

These fully calibrated data sets are then fed to the third stage of the pipeline, which combines exposures across different channels and sub-bands into a final drizzled data cube. The parameters for the third stage of the pipeline were mostly left unchanged, except changing the outlier threshold at 99 per cent. During the first stage of the pipeline, a pixel atop a bright trace of a source might get flagged as `DO_NOT_USE`. During the cube building in stage-3, values then have to be interpolated from other dither positions that may have a different centre, resulting in absorption-like drop outs in the spectrum. To avoid such effects, we turned on the `pixel_replace` step in the third stage of the pipeline (in the earlier versions of the pipeline, this parameter used to be in the second stage).

The final data products consist of 12 data cubes, corresponding to each channel (1, 2, 3, and 4) and the respective sub-bands (SHORT, MEDIUM, and LONG configurations), providing a continuous wavelength coverage between 4.9 and 27.9 μm.

2.2 Archival ALMA and VLT/MUSE observations

The *JWST*/MIRI-MRS observations described in Section 2.1 trace the warm phase (∼100–1000 K) of the molecular gas. However, molecular gas also exists in the cold gas phase, observable at mm/sub-mm wavelengths, and the different sources of ionization (star formation/AGN) can be inferred from diagnostics in optical spectra (e.g. BPT diagrams: S. Veilleux & D. E. Osterbrock 1987). Therefore, we complemented our *JWST*/MIRI-MRS observations with resolved sub-mm observations from ALMA and archival optical IFS observations from VLT/MUSE.

We used Phase-3 ESO data release portal to retrieve the fully processed MUSE data cubes. IR20551 was observed with MUSE on 2015 September 10 as a part of a GTO programme (ID 095.B-0049, PI: Soto). The average seeing during the observations was ∼1.5 arcsec, as recorded in the observatory logbooks. The spatial resolution of MUSE observation is ∼1.3 arcsec, derived from the full width at half-maximum (FWHM) of the isolated stars in the MUSE field of view. The IR20551 MUSE data cube has a field of view of $\sim 1.2 \times 1.2$ arcmin^2 with a spaxel sampling of 0.2×0.2 arcsec^2. The spectral axis provides a contiguous wavelength coverage in the optical from 0.465–0.93 μm, with a spectral resolving power ranging from 2000 at the shortest wavelengths to 4000 at the long wavelength end.

Archival ALMA CO(2-1) observations of IR20551 were obtained from the programme 2022.1.01262.S (PI: J. Ueda). Observations were done in two separate configurations covering baselines up to ∼ 2.6 km (TM1) and ∼ 0.6 km (TM2), with array angular resolution of ∼ 0.06 and ∼ 0.26 arcsec, and maximum recoverable scales of ∼ 1.0 and ∼ 3.7 arcsec, respectively. We recreate the calibrated measurement sets (MSs) using CASA pipeline version 6.5.4-9-pipeline-2023.1.0.124 (CASA Team 2022). Each MS was trimmed down to contain only the UV visibilities from the spectral window containing the CO(2-1) line, afterwards the zeroth-order polynomial fit to the continuum emission in the spectral window was then subtracted using the `uvcontsub` task. We perform imaging of the CO(2-1) line in 4.5 km s^{-1} channels combining data from both MSs with `tclean`, adopting Briggs weighting (D. S. Briggs 1995) with robust of 2.0, `auto-multithresh` masking (A. A. Kepley et al. 2020), and the `multi-scale` deconvolver (T. J. Cornwell 2008) to model emission on scales of 0.1, 0.5, 1.0, and 3.0 arcsec. We use the interactive mode to visually inspect and manually edit the cleaning mask generated at each cycle as needed, until the cycle threshold reaches $\sim 3\sigma_{\rm RMS}$, where $\sigma_{\rm RMS} = 0.44$ mJy beam^{-1} is the per channel root-mean-square value measured within an emission free region in the dirty cube (i.e. before deconvolution). We then repeat the above process but with the `hogbom` deconvolver (J. A. Högbom 1974) to clean more deeply until the residual level reaches $\sigma_{\rm RMS}$ (see A. K. Leroy et al. 2021). The final CO(2-1) cube has a synthesized beam of 0.12×0.10 arcsec^2. Lastly, we smooth the primary beam-corrected CO cube to a Gaussian beam with FWHM of 0.8 arcsec and re-grid the cube to match the worst spatial resolution of the MRS data in Channel-4.

3 DATA ANALYSIS

In this section, we describe the spectral analysis tools to model the continuum and emission lines in MRS, ALMA, and MUSE data.

3.1 Modelling warm molecular gas transitions in MRS data

The MRS data span a large range of wavelength: 4.7–26.7 μm across all four channels, each of which has a different spaxel

Downloaded from https://academic.oup.com/mnras/article/549/1/stag781/8664325 by Instituto de Astrofisica de Canarias user on 26 June 2026

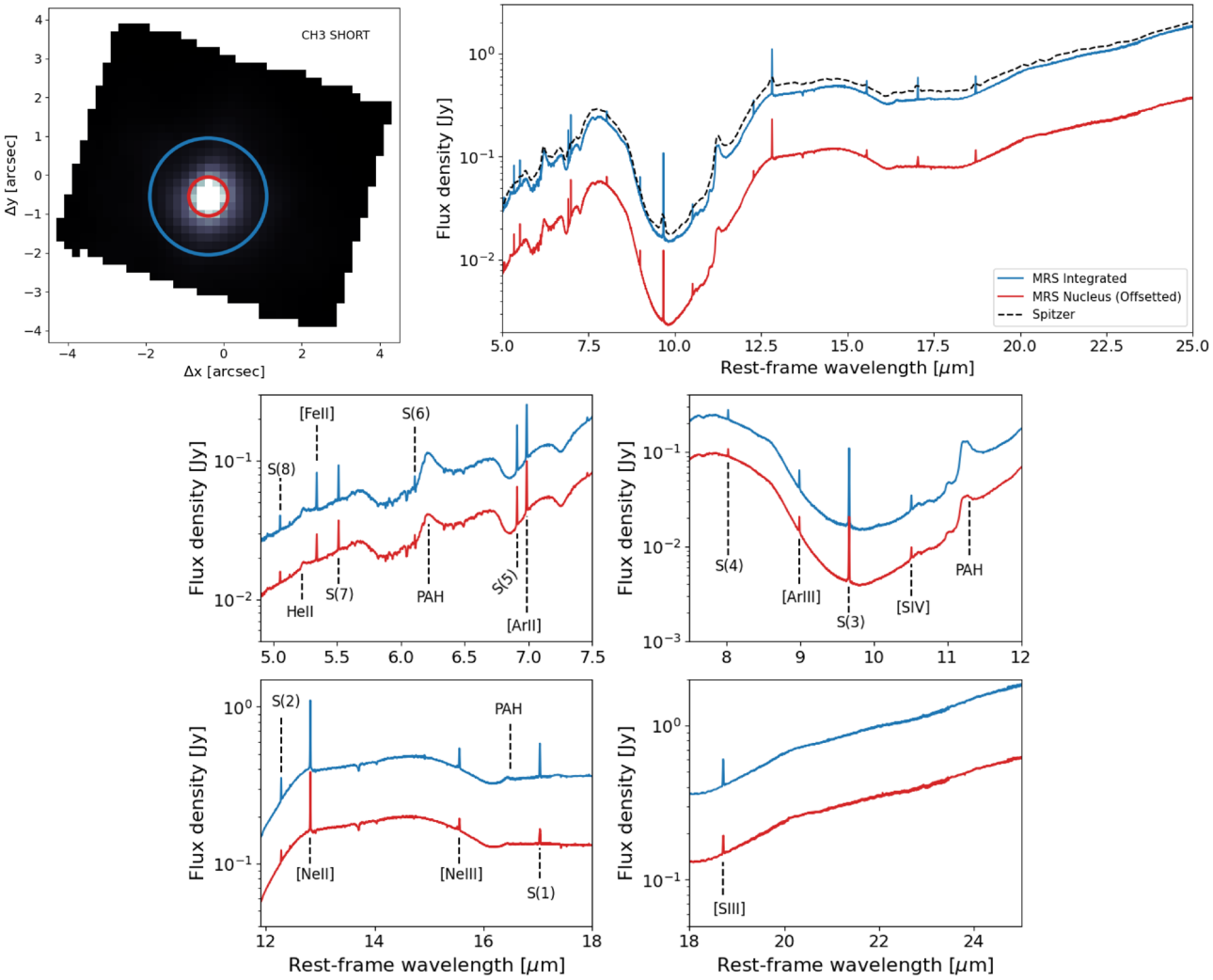


Figure 2. The top left panel shows the median MRS image of IR20551 in Channel-3. The smaller red and larger blue circle show the apertures of extraction for nuclear ($R = 0.5$ arcsec) and integrated spectra ($R = 1.5$ arcsec), respectively. The top right panel shows the full MRS spectra from all four channels from the nuclear (red) and integrated (blue) apertures. The nuclear aperture is offset by an arbitrary factor for better visualization. Archival *Spitzer* spectra of IR20551 is shown as black dashed line, which showcases the improvement in the quality of spectra with *JWST*/MIRI-MRS. The MRS spectra of IR20551 shows a combination of narrow lines, PAH emission, and silicate absorption features at $\sim$ 6.2m and $\sim$ 9.7 μm. The bottom four panels show the same spectra as the top right panel, but zoomed in on four different regions of the MRS spectra and the strong emission line features labelled. Rotational transitions of H_2 (S(1)–S(8)) are detected, along with PAH and low-ionization lines such as [Ne II]. High-ionization emission lines such as [Ne V]14.322 are not detected or are weak (see also Fig. A2).

scale, spectral resolution, and field of view. Our analysis is broken down into two steps: We first extract the spectra from each MRS cube (Channels 1–4: short, medium, and long) using two circular apertures with radii 0.5 and 1.5 arcsec (corresponding to physical scales of ≈0.4 and 1.3 kpc, respectively), which we call nuclear and integrated spectra. The continuum levels of the extracted spectra from different channels/sub-channels do not perfectly align with each other. To correct this, we stitched the spectra together by adjusting the continuum levels across channels, using the lower channel as the reference. Using these aperture spectra, we get a first-order idea of the characteristics of the mid-infrared spectrum of IR20551, such as the presence of polycyclic aromatic hydrocarbon (PAH) emission, silicate absorption features, and relevant emission lines such as the H_2 rotational transitions. We also compare the nuclear and integrated spectra with archival *Spitzer*/IRS spectra and demonstrate the incredible improvement in depth and spectral resolution of MRS compared to these archival spectra. We then focus on fitting the individual warm molecular hydrogen rotational transitions with a Gaussian model in the nuclear and integrated spectra, followed by a spatially resolved pixel-by-pixel analysis of these lines.

The spectra extracted from the nuclear ($R = 0.5$ arcsec) and integrated ($R = 1.5$ arcsec) apertures are shown in Fig. 2. To model the continuum emission in each spectra, we use a modified version of the `cafe` software[1] (see J. A. Marshall et al. 2007; T. S. Y. Lai et al. 2022; L. Armus et al. 2023; T. Diaz-Santos et al. 2025) that was originally adopted for *Spitzer*/IRS data and is currently being updated for *JWST*. `cafe` simultaneously models the PAH emission, dust continuum, silicate absorption, and the narrow fine structure atomic and molecular gas emission lines. As the main focus of our paper is to analyse the warm molecular gas

[1] https://github.com/GOALS-survey/CAFE

Downloaded from https://academic.oup.com/mnras/article/549/1/stag781/8664325 by Instituto de Astrofisica de Canarias user on 26 June 2026

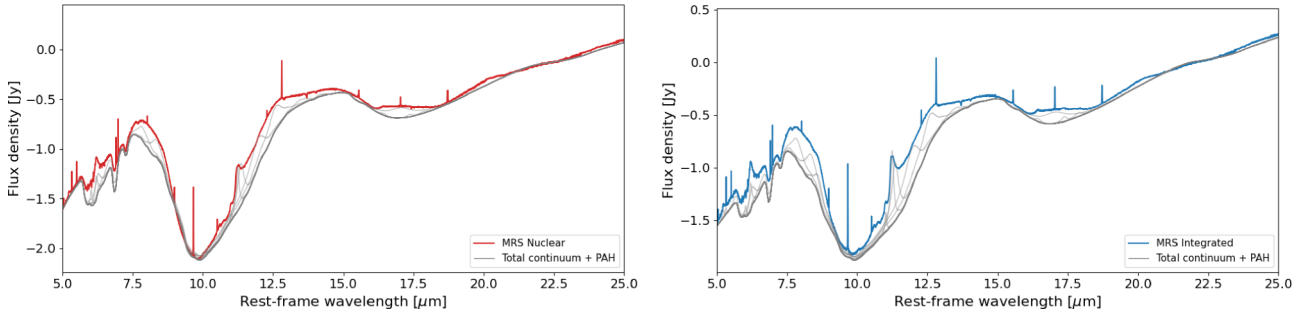


Figure 3. The nuclear (left) and integrated (right) MRS spectra of IR20551, with the total continuum model and PAH emission line fits from `cafe` overlaid. The individual components from AGNs, starburst, hot, warm, and cold dust, etc. are not shown due to high degree of degeneracy between these different components. The `cafe` model reproduces the overall mid-infrared continuum well, along with the PAH emission and silicate absorption features.

transitions, we model the overall continuum emission, without a detailed decomposition into individual contributions from the AGN, starburst, or different dust components. As there are many components, such continuum decompositions are also prone to degeneracies. However, based on the saturated central source in *F770W* image in Fig. 1, it is likely that the mid-infrared continuum is dominated by the central source (a putative AGN) in IR20551. Fig. 3 shows the mid-infrared continuum and PAH components in the nuclear and integrated MRS spectra of IR20551.

After fitting the underlying mid-infrared continuum, we focus on modelling the rotational transitions of the H_2 molecule in the nuclear and integrated spectra. The observed spectrum contains S(1)–S(8) H_2 transitions, with their expected wavelengths (based on the redshift of IR20551) listed in Table 1. Although the `cafe` software models these individual H_2 and other ionized emission lines in the spectra, there are significant residuals at the location of these emission lines. Therefore, we only use the overall continuum models from `cafe` , and use a custom script to model the S(1)–S(8) H_2 lines after subtracting the overall continuum. Each H_2 line is fitted with a single Gaussian function around spectral windows within ± 0.03 μm of the respective line centres. We did not add additional Gaussians, based on minimal changes in the Bayesian Information Criterion (BIC; see G. Schwarz 1978) values between single and multiple Gaussian models. The H_2 emission lines largely exhibit narrow profiles with no apparent red or blue wings. To estimate the uncertainties on the derived parameters, we generated 100 mock spectra by adding rms noise to the modeled spectrum and repeated the line-fitting procedure for each realization. The standard deviation of the resulting parameter distributions was then adopted as the error estimate. The H_2 emission line profiles and the corresponding Gaussian fits for the nuclear and integrated aperture spectra are shown in Fig. 4. The parameters of the Gaussians fits (line centroid, FWHM, and flux) are reported in Table 1. The reported line widths (FWHM) in Table 1 are corrected for the instrumental LSF.

We also fit each H_2 line spaxel-by-spaxel with a single Gaussian function and using the parameters from the integrated line fitting as a prior. For these spaxel-by-spaxel fits, we allow the line widths and the line centroids to vary in order to reproduce the variation in the H_2 line profiles due to galaxy rotation and/or turbulence. We note that IR20551 is a late-stage merger and therefore we expect turbulence in gas kinematics, especially in the central regions. The output of the spaxel-by-spaxel fitting consists of the line centroid, width, and flux map for each H_2 transition. We show the maps for S(2) and S(7) transitions as examples in Fig. 5. The rest of the H_2 transitions show similar morphological and kinematic structure as S(2) and S(7).

3.2 Resolved CO(2-1) characterization with ALMA

The ALMA data cubes for CO(2-1) characterization were already continuum-subtracted during the re-imaging procedure described in Section 2.2. To model the cold molecular gas using the CO(2-1) emission line, we follow the same procedure as modelling the H_2 emission lines in the mid-infrared spectra i.e. use multiple Gaussian functions based on the BIC criterion. Given the high spectral resolution of ∼4.5 km s^{-1}, we were able to resolve the CO(2-1) emission lines down to the asymmetries in the emission line profile. At most two Gaussians were required to reproduce the CO(2-1) line profile. The CO(2-1) spectra extracted from a circular aperture of radius 1.5 arcsec and the multi-Gaussian model is shown in Fig. 6. The radius of 1.5 arcsec was chosen to match the integrated spectrum in the MRS data. For the two-Gaussian model used here, we use a non-parametric approach, which is commonly used in the literature (see C. M. Harrison et al. 2014; D. Kakkad et al. 2020; D. Wylezalek et al. 2020, for details). We derive the following parameters with CO(2-1): v_{50}, w_{80} ($v_{90} - v_{10}$) and the total flux of the two Gaussian profiles. v_X represents the velocity value containing X per cent of flux, when integrating over the line emission from the blue-end of the spectrum. For instance, v_{50} means the velocity value containing 50 per cent of the total flux of the emission line and is an indicator of the centroid velocity of the entire line profile. w_{80} is a measure of the FWHM of the line, when using multiple Gaussian functions. The CO(2-1) line model parameters v_{50} and w_{80} and flux are −90 and 200 km s^{-1}, respectively. We also repeat the fitting procedure for each spaxel to arrive at the maps showing the distribution of the velocity centroids, widths, and the CO flux, shown in Fig. 7.

We note that the spatial resolution, pixel scales, and the field of view differ between each MRS channels, which further differ from that of the ALMA CO(2-1) observations, with which we aim to compare the warm molecular characteristics. To derive the warm H_2 excitation maps and CO-to-H_2 flux maps, it is essential that the data sets used have the same angular resolution and the pixel scales. In order to make sure that we make an accurate comparative study between two data sets, we convolve the higher resolution data with that of the lower resolution data with a Gaussian kernel and rebin the data to match the spaxel scales between the two. For example, ALMA CO(2-1) data have an

Downloaded from https://academic.oup.com/mnras/article/549/1/stag781/8664325 by Instituto de Astrofisica de Canarias user on 26 June 2026

Table 1. Basic properties of the emission lines measured in the MRS spectra of IR20551 from apertures of radii, R = 0.5 and 1.5 arcsec. (1): emission-line feature, (2): the rest-frame wavelength of the line in μm, (3), (4), and (5): observed velocity offset of the emission line from the expected location based on its redshift (determined from the location of [O III]λ5007 line in the optical MUSE spectra), line width (FWHM, corrected for the spectral resolution) and line flux within the 0.5 arcsec aperture, (6), (7), and (8): same as (3), (4), and (5), respectively, but within the 1.5 arcsec aperture. The quoted errors indicate 1σ uncertainty.

		$R = 0.5$ arcsec			$R = 1.5$ arcsec		
Line	λ_{rest}	Δv_{obs}^{offset}	FWHM	Flux	Δv_{obs}^{offset}	FWHM	Flux
	μm	km s^{-1}	km s^{-1}	10^{-14} erg^{-1} s^{-1} cm^{-2}	μm	km s^{-1}	10^{-14} erg^{-1} s^{-1} cm^{-2}
(1)	(2)	(3)	(4)	(5)	(6)	(7)	(8)
0–0 S(8)	5.053	−12	194±4	1.14±0.02	−12	186±11	1.69±0.07
0–0 S(7)	5.511	−30	189±2	4.87±0.05	−30	193±2	6.93±0.07
0–0 S(6)	6.110	52	203±15	2.22±0.24	52	186±10	2.70±0.14
0–0 S(5)	6.910	−23	187±3	8.69±0.10	16	190±3	13.13±0.12
0–0 S(4)	8.025	−26	185±4	4.15±0.08	−26	188±4	6.63±0.11
0–0 S(3)	9.665	−11	228±3	10.32±0.12	−11	212±3	26.91±0.25
0–0 S(2)	12.279	−28	182±5	3.54±0.06	−28	189±2	10.07±0.13
0–0 S(1)	17.035	−37	217±6	4.91±0.14	−37	221±5	17.67±0.41

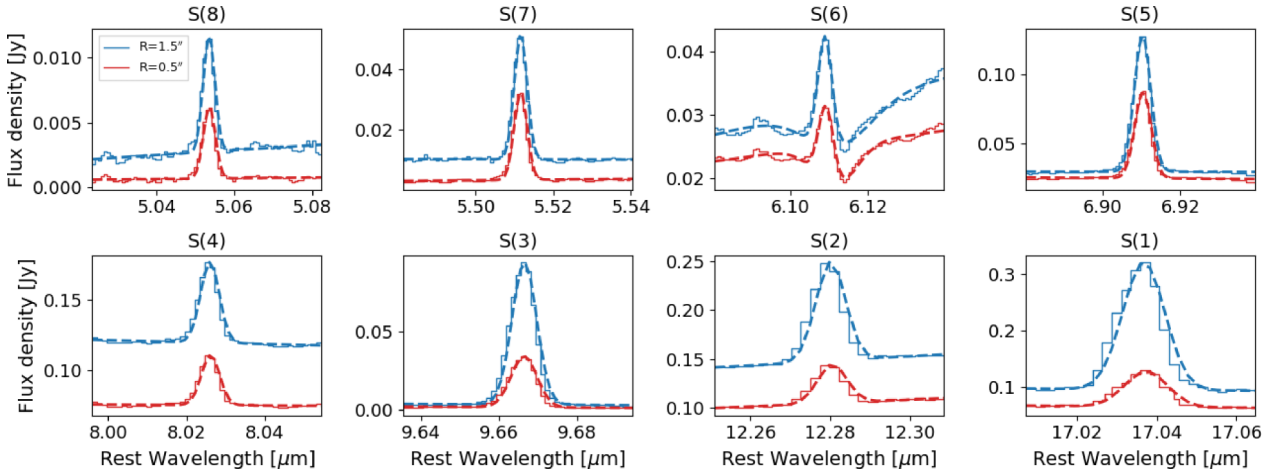


Figure 4. Rotational hydrogen lines (S(1)–S(8)) from the nuclear (solid red) and integrated (solid blue) spectra and respective single Gaussian fits (dashed lines). The rotational transitions do not show any asymmetry and are reproduced using a single Gaussian function, suggesting that there is no evidence for fast-moving warm molecular gas associated with an outflow. S(6) line is affected by an absorption feature towards the right of the profile from the instrument, which is well fit with an inverted Gaussian component.

angular resolution of ∼0.3 arcsec, while Channel-3 of the MRS, which contains the H_2 0–0 S(2) emission line, has an angular resolution of ∼0.8 arcsec.[2] Therefore, when deriving the flux ratio map, we convolve CO(2-1) map with a Gaussian kernel to match the angular resolution of the MRS cube, which has a lower spatial resolution.

3.3 Resolved BPT maps with VLT/MUSE

The main purpose of incorporating the MUSE optical spectroscopy in this study is to determine the dominant source of ionization (AGN, star formation, or composite) in the central region of IR20551, as inferred from emission-line ratios, using a spatially resolved BPT diagrams (e.g. J. A. Baldwin, M. M. Phillips & R. Terlevich 1981; S. Veilleux & D. E. Osterbrock 1987; D. Kakkad et al. 2022), and to compare the [O III]5007 emission-line profile, tracing diffuse warm ionized gas, with the molecular gas tracers described in Sections 3.1 and 3.2. We focus on the [N II]and [O I] BPT diagrams, which requires accurate measurements for the following lines: Hβ, [O III]λ5007, Hα, [N II]λ6585, and [O I]λ6300. Before carrying out the spaxel-by-spaxel fitting, we first inspect the optical spectra extracted from a 1.5 arcsec aperture [comparable to the integrated MRS and CO(2-1) spectra described in Sections 3.1 and 3.2, respectively] centred on the AGN location. This allows us to identify the detected lines and assess whether they exhibit asymmetries indicative of outflows. The integrated spectra of [O III]and Hα lines are presented in the top panels of Fig. 8 as examples, showing tentative evidence for a blue wing in the [O III]5007 and Hα line profiles.

To model these spectra, we first subtract the contribution from the stellar continuum in the optical spectra using penalized pixel fitting routine (`ppxf` ; see M. Cappellari & E. Emsellem 2004; M. Cappellari 2017), implemented within the `lzifu` software (see I. T. Ho et al. 2016; K. Kreckel et al. 2018). During the `ppxf` fitting procedure, we masked the emission lines, regions contaminated by sky lines, and telluric absorption features. After subtracting the stellar continuum emission, we fit the emission lines using Gaussian functions along with a linear function that takes

[2] https://jwst-docs.stsci.edu/jwst-mid-infrared-instrument/miri-operations/miri-dithering/miri-mrs-psf-and-dithering

Downloaded from https://academic.oup.com/mnras/article/549/1/stag781/8664325 by Instituto de Astrofisica de Canarias user on 26 June 2026

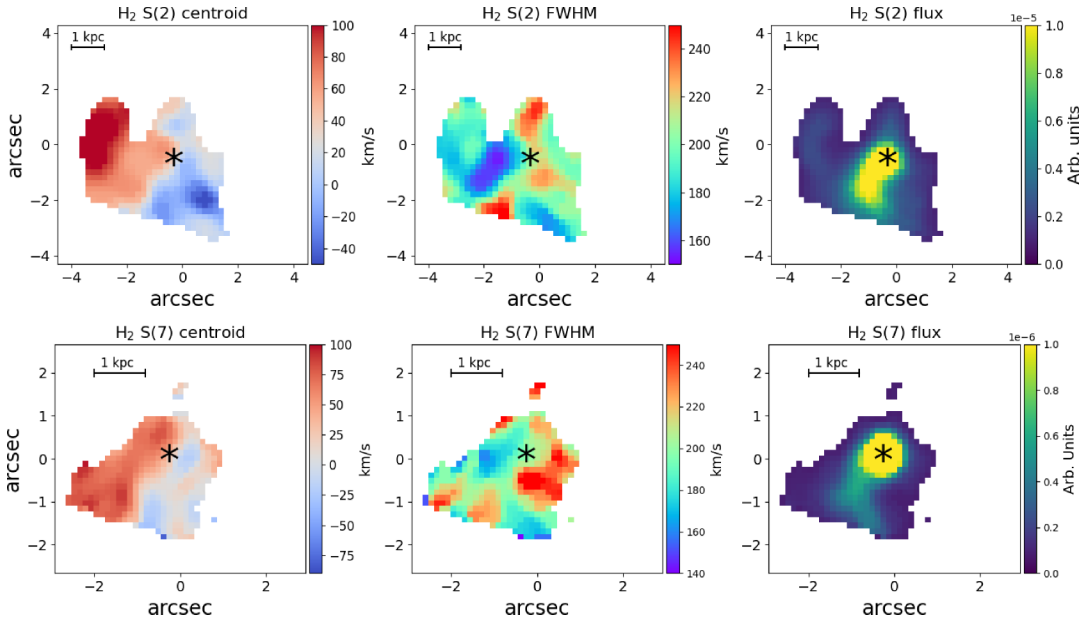


Figure 5. Maps showing the variation in the centroid (left panels), width (FWHM, middle panels), and flux (right panel) of the H_2 rotational transitions, S(2) (top panels) and S(7) (bottom panels) as examples. The maps showcase the presence of two tidal tails in the central region of IR20551 – one towards the NE and other towards the SE. S(7), a higher excitation line, is covered in the lower channels of MRS, which have a smaller field of view. Therefore, the tidal tail towards the NE of the nucleus, seen in S(2), is not visible. The black star in all plots mark the location of the nucleus (putative AGN). See Section 4.2 for more details about these maps.

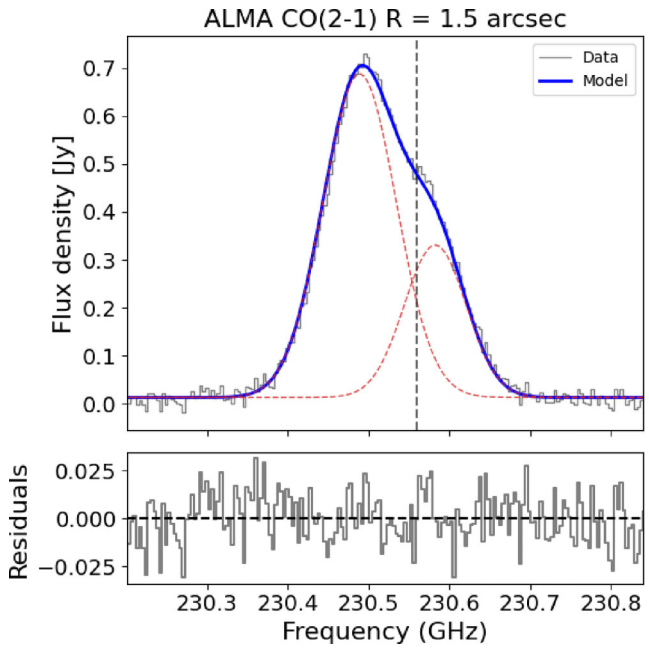


Figure 6. The grey step curve in the top panel shows the extracted CO(2-1) spectra from the ALMA data cube (radius of aperture, $R = 1.5$ arcsec) and the smooth solid blue curve overlaid shows the total multi-Gaussian model. The dashed red curves show the individual Gaussians. The vertical line shows the expected location of CO(2-1) line based on the redshift of IR20551. The bottom panel shows the residuals from the fit. The w_{80} parameter for the total Gaussian fit is ∼200 km s^{-1}, which does not suggest the presence of a fast moving cold molecular gas outflow in IR20551.

into account any residual underlying continuum emission in the spectra. Similar to the procedure adopted for the mid-infrared H_2 and sub-mm CO lines, the number of Gaussian functions used was decided based on the BIC values. A maximum of two Gaussians was required to reproduce the emission lines. We employ additional constraints while performing these Gaussian fits, such as setting the emission-line ratio [O III]λ5007:[O III]λ4959 = 3:1 and coupling the centroid locations of all emission lines based on their expected locations in the spectra. Further details about these constraints are available in D. Kakkad et al. (2022).

We repeat this procedure for each spaxel to construct flux maps of Hβ, [O III]5007, Hα, and [N II]6585, shown in the bottom panels of Fig. 8. We also calculate v_{50} and w_{80} values for the [O III]emission line in each pixel. The [O III]v_{50} and w_{80} maps are shown in the left and right panels of Fig. 9, respectively. The blue colours in the [O III]v_{50} map represent the blue-shifted velocities, while the red colours show the red-shifted velocities. Similarly, the blue colours in the [O III]w_{80} map show regions with low velocity dispersion (close to the limit of the MUSE spectral resolution), while the red colours show regions with high velocity dispersions. Since our focus is on constraining the dominant ionization mechanism, we consider only the total line flux, without separating the narrow and broad Gaussian components. The [N II]/Hα flux ratio map is presented in the top left panel of Fig. 10, while the distribution of individual pixels in the [N II]-BPT diagram is shown in the top right panel. We also show the [O I]/Hα map and the distribution of individual pixels in the [O I]-BPT diagram in the bottom panels of Fig. 10. We discuss these flux and velocity maps further in Section 4.

Downloaded from https://academic.oup.com/mnras/article/549/1/stag781/8664325 by Instituto de Astrofisica de Canarias user on 26 June 2026

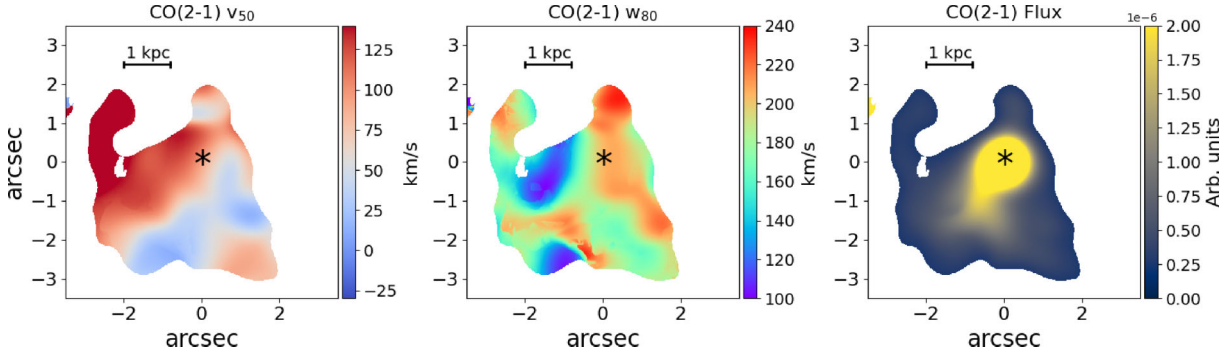


Figure 7. CO(2-1) maps of IR20551: v_{50}, which is equivalent of a centroid map is shown in the left panel, the middle panel shows the w_{80} map (equivalent of an FWHM map), and the right panel shows the flux map. Non-parametric measurements are shown here due to the double Gaussian fitting in CO(2-1) lines. The black star in the centre of the images marks the putative AGN location. The centroid, width, and morphology mirror the warm molecular gas transitions shown in Fig. 5, suggesting that the two molecular gas phases show similar morphological and kinematic properties.

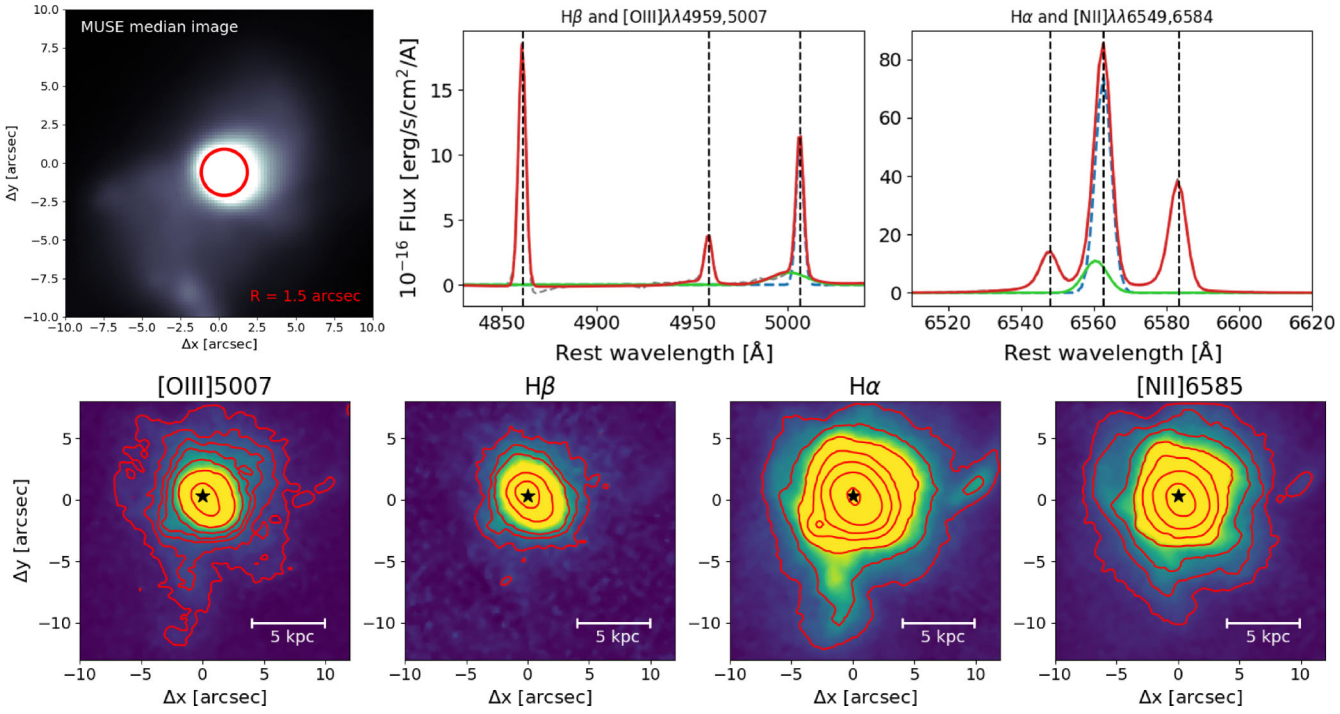


Figure 8. The top left panel shows the median MUSE image of IR20551 and the red circle shows the aperture of optical spectral extraction ($R = 1.5$ arcsec), similar to the aperture radii used for MRS integrated and ALMA CO(2-1) data. The top middle and right panels show the extracted MUSE spectra with emission line model fits, zoomed in on Hβ, [O III]$\lambda\lambda$4959, 5007 (middle panel), Hα, and [N II]$\lambda\lambda$6549, 6585 (right panel). The background grey curve in the top middle and top right panels is the original data, the red curve shows the overall fitting, the dashed blue curve shows the first Gaussian component (narrow), and the solid green line shows the second Gaussian component (broad). The bottom panels show the flux maps of these emission lines with red contours added for visualization of the most extended low surface-brightness line emission. H α emission shows a second clump to the SE of the AGN location, which is a star-forming region confirmed via BPT map in Fig. 10.

4 RESULTS

In this section, we present the results from the multiwavelength imaging and spectroscopic data of IR20551, focusing on the source of ionization, the mass and temperature of the warm molecular gas, and its comparison with the cold molecular gas mass.

4.1 Ionization source in the central region of IR20551

Feedback from starbursts and/or AGN is thought to either expel a galaxy's molecular gas or heat it, thereby suppressing future star formation. ULIRGs such as IR20551 are expected to produce strong feedback, given their high infrared luminosities, ongoing or previous mergers, and the possible presence of an AGN. In the case of IR20551, we analyse its dominant ionization source in the central 5 × 5 arcsec^2, the area covered by the MRS.

Rest-frame optical *HST*/ACS *F*814*W* and near-infrared *JWST*/NIRCam *F*277*W* imaging reveal the large-scale structure of IR20551, a late-stage merger with a prominent tidal tail extending SE of the nucleus and a faint tail to the NW (see top panels of Fig. 1). The NW tidal tail is better visible in the MIRI image (which is rather obscure in the *HST* and NIRCam images), suggesting an abundance of dust in the tidal tail. Zooming

Downloaded from https://academic.oup.com/mnras/article/549/1/stag781/8664325 by Instituto de Astrofisica de Canarias user on 26 June 2026

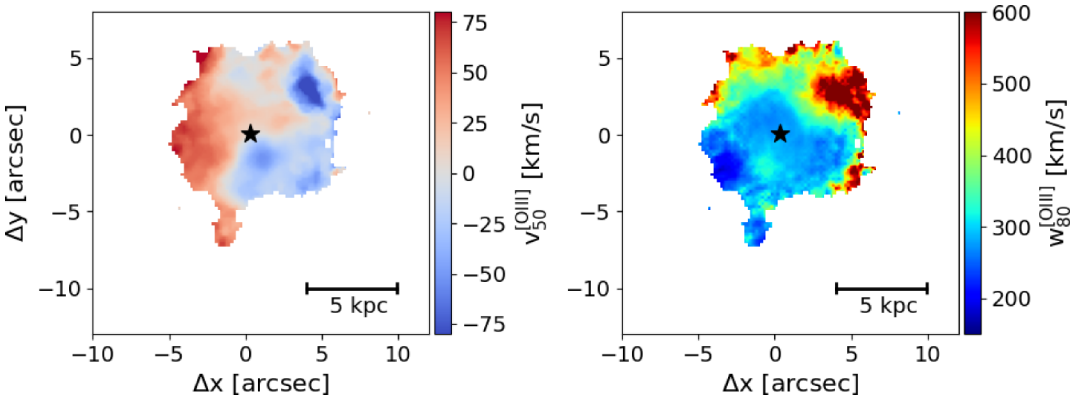


Figure 9. The left panel shows the [O III]v_{50} map and the right panel shows the [O III]w_{80} map from two-Gaussian fits to VLT/MUSE data described in Section 3.3. The colour coding on the left panel shows [O III]v_{50} values, ranging from −75 (blue) to 75 (red) km s^{-1} and the colour coding on the right panel shows [O III]w_{80} values, ranging from ∼150 (blue) to ∼600 km s^{-1}. Neither maps show ordered motions, suggesting that the [O III]emission traces turbulent warm ionized gas in IR20551. Outflows are apparent from high w_{80} values (>500 km s^{-1}) in parts of the field. The black star marks the location of the putative AGN.

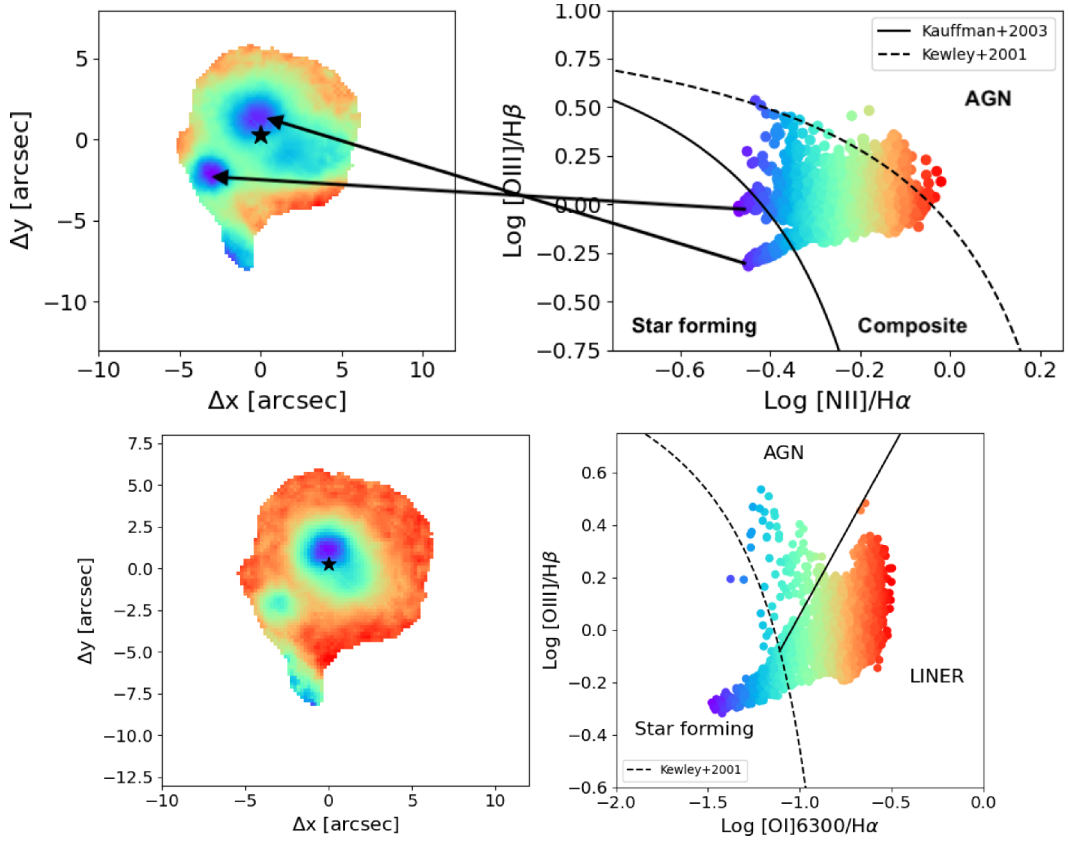


Figure 10. Top panels: the left panel shows the [N II]/Hα map of IR20551 within the central 10 × 10 arcsec^2 region and the right panel shows the corresponding [N II]-BPT diagram ([O III]5007/Hβ versus [N II]6549/Hα). The colour coding shows the [N II]6549/Hα ratio, ranging from 0.35 (dark blue) to 0.9 (red). The dashed line in the right panel indicates the line ratios for the most extreme (high-ionization) starbursts (L. J. Kewley et al. 2001b, 2013) and the solid line shows the demarcation between the star formation and 'composite' ionization processes (star formation + AGN) (G. Kauffmann et al. 2003). The location very close to the central nucleus (putative AGN marked by black star) is consistent with an H II region, along with another clump 5 arcsec to the SE of the centre. The location of these two regions in the BPT diagram is shown by arrows. The bright nuclear star-forming clump accounts for the classification of IR20551 as an H II region in the literature (L. J. Kewley et al. 2001a). The rest of the field of view is dominated by composite ionization processes. Bottom panels: the left panel shows the [O I]/Hα map of IR20551 within the central 10 × 10 arcsec^2 region and the right panel shows the corresponding [O I]-BPT diagram ([O III]5007/Hβ versus [O I]6300/Hα). The colour coding shows the [O I]6300/Hα ratio, ranging from 0.05 (dark blue) to 0.25 (red). The dashed line in the right panel indicates the line ratios for the most extreme (high-ionization) starbursts (L. J. Kewley et al. 2001b, 2013) and the solid line shows the demarcation between the star formation and 'composite' ionization processes (star formation + AGN).

Downloaded from https://academic.oup.com/mnras/article/549/1/stag781/8664325 by Instituto de Astrofisica de Canarias user on 26 June 2026

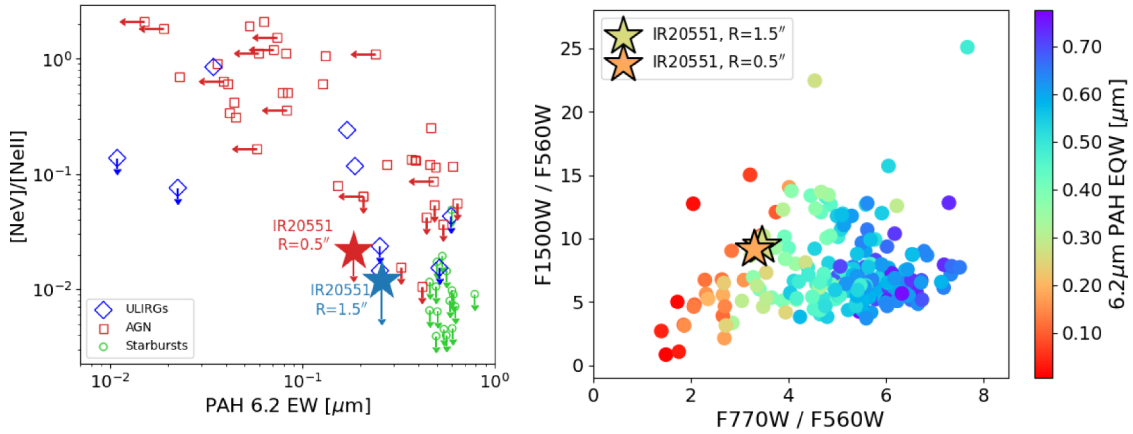


Figure 11. Mid-infrared AGN diagnostics: left panel: flux ratio [Ne V]14.3/[Ne II]12.8 versus PAH 6.2 μm EW. The red squares show AGNs (from Y. Wu et al. 2009; S. Tommasin et al. 2010), blue diamonds show ULIRGs (L. Armus et al. 2007), and green circles show the location of starburst galaxies (J. Bernard-Salas et al. 2009). The location of IR20551 spectra from the two apertures, $R = 0.5$ arcsec and 1.5 arcsec, are shown as red and blue stars, respectively, based on upper limits on [Ne V] flux. The location of IR20551 is consistent with the range expected for AGNs and ULIRGs and is somewhat shifted from the starburst regime (by a factor of 1/3). Right panel: $F1500W/F560W$ versus $F770W/F560W$ flux density ratio plot showing the location of the nuclear ($R = 0.5$ arcsec) and integrated ($R = 1.5$ arcsec) regions of IR20551 with respect to LIRGs in the parent GOALS sample (S. Stierwalt et al. 2013). The parent LIRG sample are colour-coded by the 6.2 μm PAH EW. Its strength tends to be anticorrelated with the strength of an AGN continuum. The red and orange regions in the plot are systems dominated by AGN emission. Based on the two diagnostic diagrams shown here, we cannot rule out the presence of AGN in IR20551.

into the central 5×5 arcsec^2 region (bottom panels in Fig. 1), the disturbed morphology in the *HST* image shows features consistent with an ongoing merger. The central bright source, however, starts becoming visible in the NIRCam image, while in the MIRI image, emission from IR20551 saturates the detector. There are no indications of a second nucleus in the vicinity of the bright source based on the *HST* and *JWST* images. The extremely bright point source in the centre may come predominantly from the hot dust continuum of a buried AGN (H. Inami et al. 2022).

Fig. 2 shows the nuclear and integrated mid-infrared spectrum of IR20551. At shorter wavelengths, absorption features are visible around 6 and 6.85 μm, which may be attributed to mixture of ices and hydrogenated amorphous carbons (D. G. Furton, J. W. Laiho & A. N. Witt 1999; J. A. Marshall et al. 2007). A deep silicate absorption feature is also visible at 9.7 μm and around 18 μm, which suggests that the central source is embedded in a smooth distribution of dust. We calculate the silicate depth at 9.7 μm, $s_{9.7\ \mu m} = \ln(f_\lambda/C_\lambda)$, where f_λ is the flux at the central wavelength of the 9.7 μm absorption feature and C_λ is the assumed continuum level at the central wavelength in the absence of the absorption feature (see H. W. W. Spoon et al. 2007). Lower values of the silicate depth imply larger absorption columns along the line of sight. We find $s_{9.7\ \mu m} = -3.22$ and -2.91 in the nuclear and integrated spectra, respectively, i.e. the absorbing column towards the central regions is larger than towards the outer regions of IR20551. The $s_{9.7\ \mu m}$ values calculated here for IR20551 is also within the range observed for GOALS galaxies in S. Stierwalt et al. (2014). These findings are also consistent with the highly obscured X-ray column density, $N_H = 8 \times 10^{23}$ cm^{-2}, reported for IR20551 in the literature (e.g. A. Franceschini et al. 2003).

We detect fine structure lines in MRS spectra from ionized atoms in IR20551, such as [Ne II] at 12.8 μm, [Ne III] at 15.5 μm, and [S III] at 18.7 μm. However, coronal lines such as [Ne V] 14.3 μm and [O IV] 25.9 μm produced by the hard radiation from an AGN are not detected or are very weak (see Fig. A2). The absence of these lines does not rule out the presence of an AGN, as their non-detection may result from heavy dust obscuration around the nucleus (see also G. H. Rieke et al. 2025). Indeed, a large dust covering fraction around an AGN can also prevent the formation of narrow-line region and consequently, the production of emission from highly ionized atoms. We calculate an upper limit on the [Ne V] 14.3 μm flux in both apertures (nuclear and integrated) and plot the flux ratio [Ne V]14.3/[Ne II]12.8 versus the EW of PAH 6.2 μm feature. The location of IR20551 compared to other ULIRGs, AGNs, and starburst galaxies is shown in the left panel in Fig. 11. IR20551 is located within the range expected for AGNs and ULIRGs and nearly a factor of 1/3 less than pure starbursts, which show strong PAH emission with high EWs and weak or no [Ne V] emission (L. Armus et al. 2007). Even if a starburst is present, the strength of PAH 6.2 μm is reduced in the presence of hot dust.

Mid-infrared colour-based diagnostic diagrams, such as $F1500W/F760W$ versus $F770W/F560W$, can also be used to distinguish whether the central source is starburst- or AGN-dominated (e.g. L. Armus et al. 2007; A. S. Evans et al. 2022). In these diagrams, lower $F770W/F560W$ ratios correspond to smaller PAH equivalent widths (EWs), indicative of AGN-dominated emission. As the MIRI image in Fig. 1 is saturated, we cannot use it to calculate these colours directly. Instead, we use the available MRS spectra to construct synthetic $F560W$, $F770W$, and $F1500W$ colours by convolving the spectra with the relevant MIRI filter throughputs. The resulting diagnostic diagram is shown in the right panel of Fig. 11. Targets with PAH EWs below 0.25 (shown in red/orange) are likely dominated by AGN activity (L. Armus et al. 2007). The nuclear and integrated synthetic photometric colours of IR20551 lie approximately between the regions characteristic of pure AGN and pure starburst systems, again suggesting that the contribution from an AGN cannot be excluded and that IR20551 is consistent with being a composite system.

Optical BPT diagnostics, on the other hand, tell a different story (see Fig. 10). The central region close to the AGN has low

Downloaded from https://academic.oup.com/mnras/article/549/1/stag781/8664325 by Instituto de Astrofisica de Canarias user on 26 June 2026

[N II]/Hα and low [O III]/Hβ emission, placing it in the star-forming region of the BPT diagram. There is a second clump towards the SE of the nucleus, also in the star-forming region of the BPT diagram, which coincides with continuum peaks in ACS/*F*814*W* and NIRCam/277*W* (see Fig. A3). The lack of optical AGN emission from the galactic nucleus could result from heavy obscuration. This is consistent with the zoomed-in *HST*/ACS *F*814*W* in the bottom left panel of Fig. 1, which does not show a prominent central point source.

Apart from these regions, the rest of the field of view in IR20551 shows 'composite' emission. This indicates that not all of the forbidden line emission off the nucleus can be produced solely by H II regions. Instead, an additional contribution appears to be present. The spiral galaxy NGC 5806 also shows a similar pattern of star-formation in its centre, surrounded by extended gas with a composite AGN + H II spectrum (e.g. S. L. Robbins, S. I. Raimundo & M. A. Malkan 2025). This non-stellar emission can be attributed to an AGN, from either a Seyfert nucleus or a LINER (see e.g. M. A. Malkan, L. D. Jensen & L. Hao 2026). The most sensitive discriminator between these two kinds of non-stellar emission is the strength of the [O I]λ6300 line. We therefore measured this line in MUSE data cube and show the spatially resolved O I-BPT diagram in the bottom panels in Fig. 10. The solid line shows the separation between Seyfert (upper) and LINER (lower) spectra. The strong [O I] line emission shows that most of the observed centre of the galaxy has a LINER spectrum – not that of a Seyfert AGN. Indeed spatially extended LINER emission is often observed in some regions of LIRGs.

The physical mechanism giving rise to LINER emission spectra is under debate, and could be either a very weak AGN, or ISM shocks in a wind. The LINER emission we see in IRAS20551 is not associated with the nucleus, and is, instead, found in outer regions that tend to have wider [O III]wings (particularly along the northern edge). We take this as weak evidence for the shock origin of the LINER emission (see also H. Sugai & M. A. Malkan 2000).

In summary, our findings here are consistent with literature classifications of this source as an H II region at optical wavelengths. However, the AGN nature of the central source cannot be excluded with diagnostic diagrams based on mid-infrared photometry and spectra. In order to investigate whether the AGN and/or starburst drives any feedback, we perform a kinematic analysis of the emission lines tracing ionized and molecular gas in the following sections.

4.2 Warm molecular gas morphology and kinematics

We detect the following H_2 rotational transitions in the MRS spectrum of IR20551: 0–0 S(1), 0–0 S(2), 0–0 S(3), 0–0 S(4), 0–0 S(5), 0–0 S(6), 0–0 S(7), and 0–0 S(8) observed at wavelengths 17.767, 12.807, 10.081, 8.370, 7.207, 6.371, 5.748, and 5.270 µm, respectively. We first summarize the H_2 detections in the nuclear and integrated spectra, before diving into the spatially resolved properties from the spaxel-by-spaxel analysis. The nuclear and integrated H_2 spectra, along with the respective Gaussian models, are shown in Fig. 4. Fig. 5 shows the line centroid (left panels), width (FWHM, middle panel), and flux maps (right panel) of S(2) and S(7) transitions (top and bottom panels, respectively) as examples.

The extinction-corrected fluxes of the individual H_2 lines are reported in Table 1 and are in the range 1.1–10.3 $\times$ 10^{-14} erg s^{-1} cm^{-2} in the nuclear spectra and 1.6–26.9 $\times$ 10^{-14} erg s^{-1} cm^{-2} in the integrated spectra. The extinction correction factors were obtained from `cafe`. The line flux maps shown in the right panels of Fig. 5 clearly show two prominent tidal tails in this system due to the ongoing merger: one towards the SE of the nucleus and another towards the NE. The NE tidal tail is not visible in the maps of higher transitions (S(3)–S(8)) due to the smaller field of view in the lower channels of MRS.

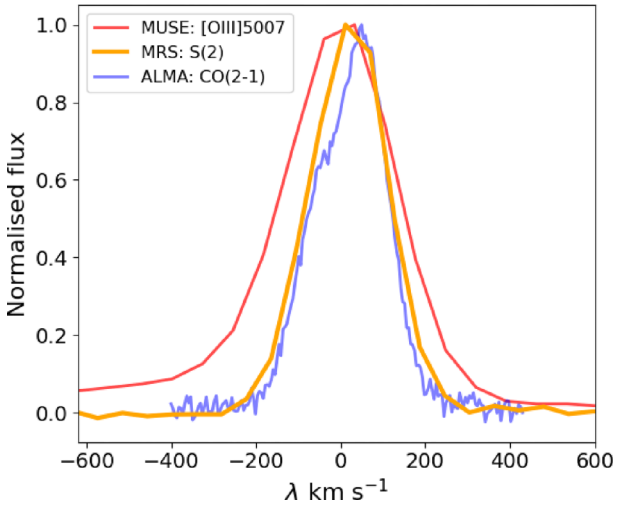


Figure 12. Normalized [O III]λ5007, H_2 S(2), and CO(2–1) line profiles plotted on the same wavelength scale. The [O III]line exhibits the largest velocity dispersion with $w_{80}^{[OIII]} \sim 790$ km s^{-1}. While the CO(2–1) profile shows mild asymmetry (see also Fig. 6), its overall width is comparable to that of the S(2) transition. These profiles point to the presence of warm ionized outflows in IR20551, whereas the cold and warm molecular gas phases show only slow-moving gas or no evidence of outflows.

The H_2 line centroid positions (based on the redshifts derived from optical lines – [O III]and Hα – in MUSE spectra) for each transition (see Table 1) show no significant variation between the two apertures, with velocity differences remaining below $\Delta v <$ 15 km s^{-1}. A comparison of the H_2 line flux maps with the centroid maps suggests that the NE tidal tail may be tracing a gas inflow towards the AGN, as indicated by the redshifted velocities seen in the left panels of Fig. 5. The centroid maps further reveal a nearly continuous velocity gradient extending from the NE to the SW of the nucleus, with the strongest redshifts located in the NE tidal tail. This relatively smooth gradient is likely a consequence of IR20551 being in a late merger stage, where the circumnuclear region begins to settle into a rotating disc.

All the H_2 transitions are spectrally resolved, with LSF-corrected line widths (FWHM) in the range ∼180–230 km s^{-1}. The median widths in the nuclear and integrated spectra are comparable, at 192 and 190 km s^{-1}, respectively. The H_2 profiles in the MRS spectra are well described by a single Gaussian component and show no evidence of extended blue or red wings in either aperture (Fig. 4). This contrasts with the [O III]and CO(2–1) profiles, which exhibit asymmetric shapes. Fig. 12 compares the [O III], CO(2–1), and S(2) lines, each normalized and plotted on the same velocity scale relative to its centroid. Among these, [O III]displays the broadest profile, with $w_{80}^{[OIII]} > 500$ km s^{-1}, suggesting the presence of outflows in the warm ionized gas phase. The presence of outflows or turbulent motion in the ionized gas is further evident from the maps in the right panel of Fig. 9, where the [O III]w_{80} values reach >500 km s^{-1}, values that cannot be explained by simple rotation. Moreover, the absence of clear

Downloaded from https://academic.oup.com/mnras/article/549/1/stag781/8664325 by Instituto de Astrofisica de Canarias user on 26 June 2026

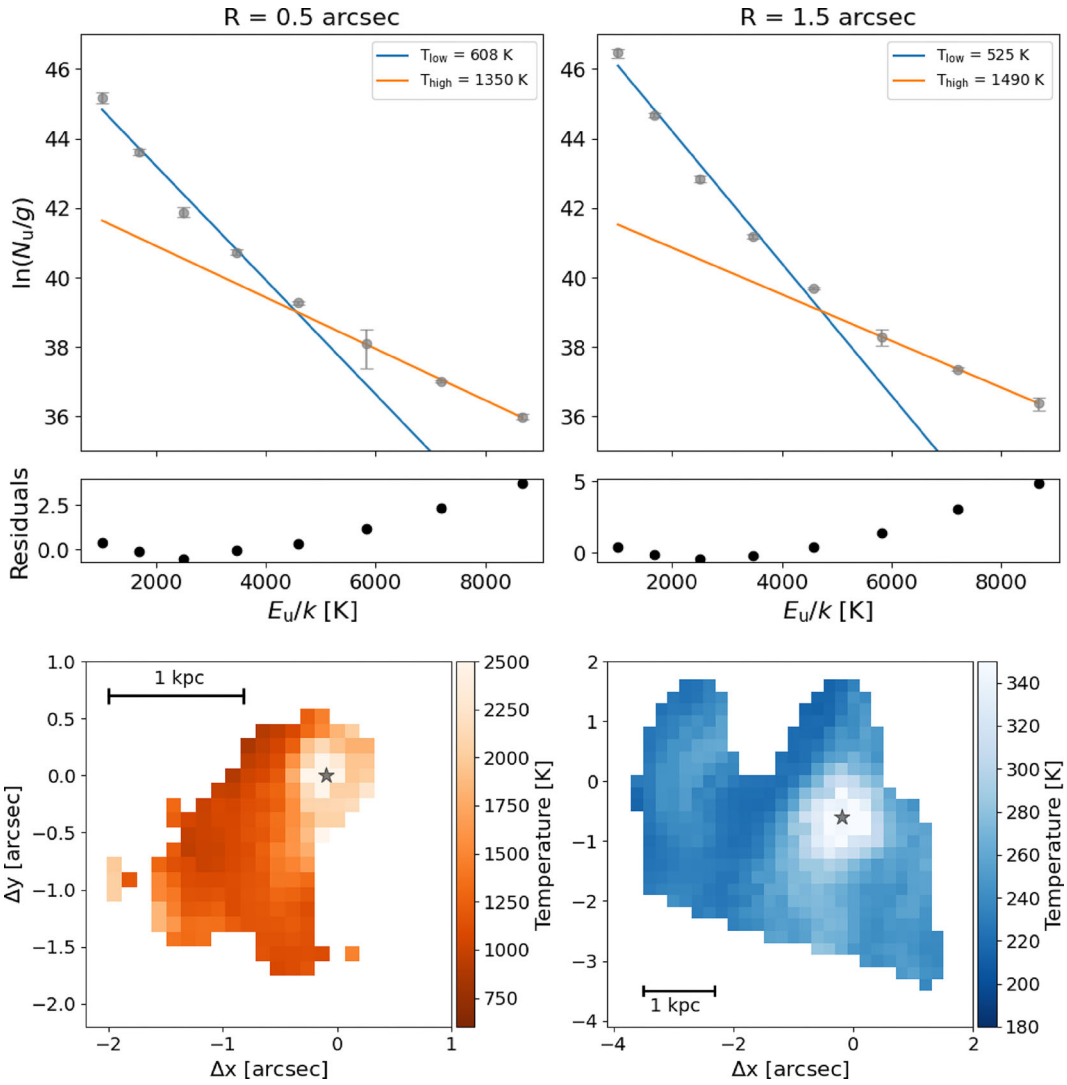


Figure 13. Top panels: temperatures derived from the nuclear (top left) and integrated (top right) spectra. The nuclear spectrum is extracted from a 0.5 arcsec circular aperture, while the integrated spectrum is taken from a 1.5 arcsec aperture, both centred on the AGN. The plots illustrate a two-temperature model for the H_2 transitions: a warm component at ≈500 K, modelled using the S(1)–S(3) lines, and a hot component at ≈1400 K, traced by the S(4)–S(8) lines. Bottom panels: the maps show the spatial distributions of the molecular gas temperature based on the two-temperature excitation models shown in the top panels. The bottom left panel shows the higher temperature and the bottom right panel shows the lower temperature distribution. The gas temperature is highest at the location of the putative AGN, consistent with it being heated by accretion activity.

structure or a coherent velocity gradient across the w_{80} map also suggests turbulence in the ionized gas. We also calculate mass outflow rates in the centre of IR20551 (using the MUSE aperture spectrum shown in Fig. 8) following the method described in D. Kakkad et al. (2022), assuming solar metallicity of the gas and calculating the electron density from the [S II]λλ6716, 6731 doublet. Assuming that the broad Gaussian component represents the outflowing gas, we find an ionized gas mass outflow rate of <0.01 $M_\odot$ yr^{-1}. The CO(2–1) line (blue curve in Fig. 12) shows mild asymmetry and requires two Gaussian components (Fig. 6), though the individual Gaussian components have modest widths of ∼120 and ∼140 km s^{-1}. These asymmetries may simply reflect turbulence in the central regions or slower moving gas compared to the ionized phase. Visually, the S(2) line in the MRS spectra has a width comparable to CO(2–1) but lacks its asymmetry, likely due to the superior velocity resolution and spectral sampling of the ALMA data. A broader discussion of these line widths in the context of outflows is presented in Section 5.

4.3 H_2 excitation in IR20551

The multiple H_2 transitions detected in the MRS spectra allow us to construct a rotation diagram of the warm molecular hydrogen, from which we can derive both the excitation temperature and, subsequently, the mass of the warm molecular gas. Warm molecular gas typically exhibits excitation temperatures of a few hundred K, making these mid-infrared transitions particularly well suited to probing CO-dark molecular gas that are not detectable at sub-mm wavelengths. In this section, we examine the temperature of the warm gas in the nuclear and integrated spectra, estimate the total warm molecular gas mass, and use the spatially resolved data to investigate the temperature distribution across the system.

Downloaded from https://academic.oup.com/mnras/article/549/1/stag781/8664325 by Instituto de Astrofisica de Canarias user on 26 June 2026

We created the rotational diagrams from the line fluxes in the nuclear and integrated spectra, following the methodology in D. Rigopoulou et al. (2002) (see also N. L. Zakamska 2010; A. Togi & J. D. T. Smith 2016; A. O. Petric et al. 2018). The top panels in Fig. 13 shows the molecular hydrogen excitation diagram of warm hydrogen, based on the H_2 line detections in the nuclear spectrum (top left panel) and the integrated spectrum (top right panel). In making these rotational diagrams, we assume the gas to be in Local Thermodynamic Equilibrium and an ortho-para ratio of 3:1. Compared to the mid-infrared spectra of IR20551 published so far in the literature (e.g. S. J. U. Higdon et al. 2006; E. Sani & E. Nardini 2012), the H_2 transitions reported in this paper probe a larger range in the upper energy levels ($E_u/k \sim$ 1000–9000 K). The excitation temperature is the inverse of the slope of the excitation diagram.

It is clear from the excitation diagram in Fig. 13 that the warm molecular gas is not well represented by a single temperature, but a range of temperatures. This is not surprising given that the molecular gas generally consists of various components at different temperatures, especially in ULIRGs, which are complex systems consisting of ionization by AGNs, star formation/starbursts, and shocks. The nuclear and integrated MRS spectra of IR20551 broadly fall into two temperature distributions, shown by the blue and orange lines in the top panels in Fig. 13: one a warm molecular gas component at an excitation temperature of ∼608 and ∼525 K and a hot gas component at an excitation temperature of ∼1350 and ∼1490 K in the nuclear and integrated spectra, respectively. The hotter phase of the gas likely probe similar gas phase as the ones traced by the rovibrational H_2 transitions in the near-infrared wavelengths (e.g. D. J. Rosario et al. 2019; R. A. Riffel et al. 2023; M. Bianchin et al. 2024).

In contrast to a two temperature model, we also used a more physical approach that models a continuous gas temperature distribution to determine warm gas mass. We fit the rotational H_2 line fluxes with a power-law temperature-dependent excitation function (see A. Togi & J. D. T. Smith 2016, for details). The A. Togi & J. D. T. Smith (2016) model assumes an upper bound on the temperature distribution at 2000 K, as the mass contribution from rotational transitions beyond this temperature is negligible. We also assume an ortho-para ratio of 3 for the statistical weights of the molecular transitions. This ratio is known to drop significantly at lower temperatures ($T \leq 30$ K, see M. G. Burton et al. 1992). However, for the warm gas temperatures considered here ($T \geq 200$ K), this assumption provides a useful conservative upper limit. We find a power-law index, $n = 4.76 \pm 0.16$, consistent with the range observed in ULIRGs (see A. Togi & J. D. T. Smith 2016) and approximately 6.1×10^8 $M_\odot$ of warm molecular gas is observed at $T \geq 200$ K in aperture $R = 1.5$ arcsec. We will compare this warm molecular gas mass with the cold molecular gas mass in Section 4.4.

We take advantage of the spatially resolved IFU data from the MRS to derive excitation maps of the warm and the hot molecular gas components. The H_2 excitation maps of the warm and the hot gas are shown in the bottom panels in Fig. 13. These maps clearly show a peak in the temperature distribution corresponding to the location of the putative AGN, with a slightly higher temperature in the NE tidal tail. The temperature distribution likely suggests that the putative AGN radiation may be the source of ionization of the warm molecular gas; however, the extended warm gas may be excited by non-AGN processes such as shocks from ionized outflows (see Section 5).

4.4 Cold gas to warm gas ratios

Most molecular gas studies in the literature focus on the cold component (T<100 K), typically traced via CO transitions at sub-mm wavelengths. The combination of ALMA and *JWST* data offers a unique opportunity to examine molecular gas abundance ratios across different temperatures, both globally and in a spatially resolved manner near the AGN. In this section, we first characterize the CO(2–1)-based cold molecular gas (total mass, morphology, and kinematics) and compare it with the warm molecular gas traced by the S(2) transition. We chose the S(2) line for comparison as its location in channel-3 of MRS provides a larger field of view than the higher excitation warm gas transitions in the lower MRS channels.

We first compare the integrated (aperture radius = 1.5 arcsec) cold and warm molecular gas masses. We derived a warm molecular gas mass of $\sim 6.1 \times 10^8$ $M_\odot$ in Section 4.3. To calculate the cold molecular gas mass from CO(2-1) line, we use the following equation from P. M. Solomon & P. A. Vanden Bout (2005):

$$L'_{CO} = 3.25 \times 10^7 \, S_{CO} \, \Delta v \, \nu_{obs}^{-2} \, D_L^2 \, (1+z)^{-3}, \quad (1)$$

where L'_{CO} is the luminosity of the CO transition measured in K km s^{-1} pc^2, S_{CO} Δv is the velocity-integrated flux in Jy km s^{-1}, ν_{obs} is the observed frequency of the CO(2-1) line (∼221 GHz) and D_L is the luminosity distance. From the integrated CO transition shown in Fig. 6, we find $L'_{CO(2-1)} = 2.8 \times 10^9$ K km s^{-1} pc^2. Assuming an excitation correction, $r_{21} = 0.4$ (see D. Iono et al. 2009; P. P. Papadopoulos et al. 2012; A. D. Bolatto, M. Wolfire & A. K. Leroy 2013), we get a cold molecular gas mass of $M_{H_2}^{cold} = 1.3 \times 10^{10}$ $M_\odot$, using an α_{CO} conversion factor of 1.8 $M_\odot$ K^{-1} km^{-1} s pc^{-2}, which is consistent with the values found for GOALS galaxies in R. Herrero-Illana et al. (2019) and within the range for ULIRGs in A. D. Bolatto et al. (2013). The ratio of cold-to-warm molecular gas mass is therefore approximately 20. In other words, >95 per cent of the molecular gas is in cold gas phase. This suggests that the central regions of IR20551 still has a vast reservoir of cold gas to continue forming stars. However, there is a non-negligible fraction of warm molecular gas (<5 per cent), possibly excited by the putative AGN and shocks (based on the excitation temperature map in the bottom panels in Fig. 13).

We use the spatially resolved data from ALMA and MRS to compare the morphology and kinematics of the cold and warm molecular gas, respectively. Fig. 7 presents the centroid velocity (left), line width (FWHM, middle), and flux (right) maps of the CO(2–1) line from the ALMA observations of IR20551. The cold gas distribution and kinematics traced by CO(2-1) are similar to that of the warm gas traced by the H_2 rotational transitions in the MRS data (Fig. 5). For instance, the CO(2-1) flux map also reveals a prominent tidal tail extending SE of the AGN, and the centroid velocity field shows a similar structure and orientation to that of the warm molecular gas. A direct comparison of the CO(2–1) and S(2) distributions is shown in Fig. 14, where the background shows the CO(2–1) emission with S(2) emission overlaid in red contours. The figure clearly demonstrates that the cold and warm molecular gas are co-spatial. Unlike some resolved multi-phase studies reported in the literature, we do not find regions in IR20551 devoid of cold molecular gas (e.g. D. J. Rosario et al. 2019; R. Davies et al. 2024).

The bottom panel in Fig. 14 shows the ratio between the flux of the CO(2-1) and S(2) line (normalized to an arbitrary scale). Note that while deriving this flux ratio map, we ensured that the spatial resolution and sampling of the two data sets are consistent

Downloaded from https://academic.oup.com/mnras/article/549/1/stag781/8664325 by Instituto de Astrofisica de Canarias user on 26 June 2026

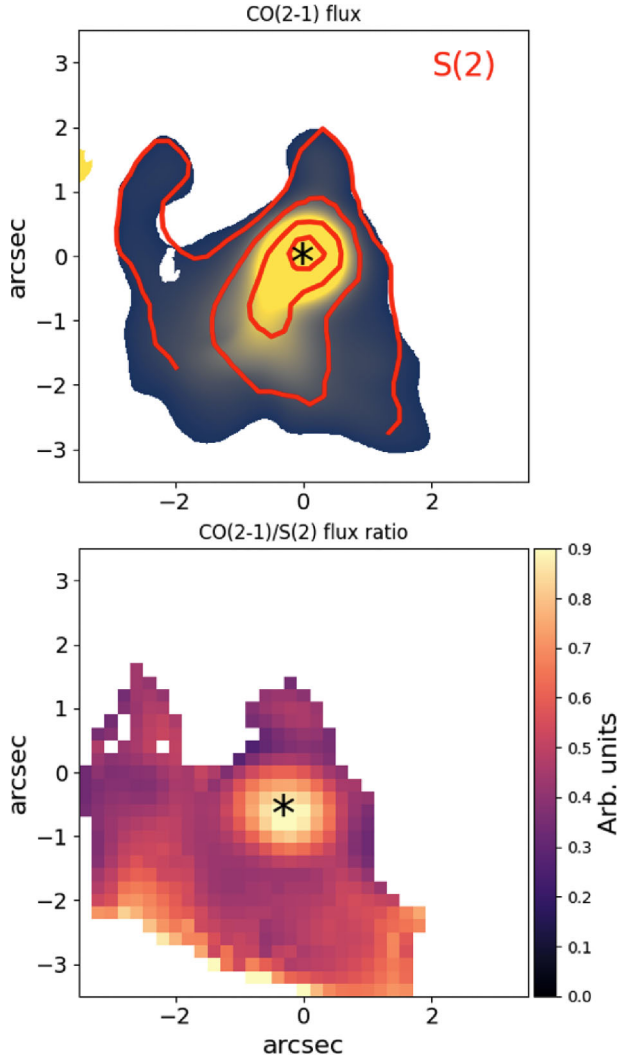


Figure 14. Top panel: the map in this plot shows the CO(2-1) flux distribution, same as the right panel in Fig. 7. Emission from the S(2) line tracing the warm molecular gas is overlaid as solid red contours at levels 10 per cent, 20 per cent, 50 per cent, and 90 per cent of the peak flux value. The map shows that the cold and warm gas are co-located in the central regions of IR20551. Bottom panel: ratio between the fluxes of CO(2-1), tracing the cold molecular gas and S(2) transition, tracing the warm molecular gas, on an arbitrary scale. The CO-based cold molecular gas dominates the mass across the field of view. The maximum ratio of cold-to-warm gas is observed in the centre, consistent with an ongoing star formation in this region.

with each other, as described in Section 3.2. We do not convert the CO(2-1) and S(2) fluxes to molecular gas masses, as the purpose of these plots is to estimate the spatial variation in the cold-to-warm gas ratio rather than deriving the exact ratios, which are affected by several assumptions such as conversion ratios or excitation corrections (which also show spatial variation, see discussion in Section 5). There is a higher fraction of cold molecular gas compared to warm gas in the centre of IR20551 and the flux ratio drops off as we move away from the centre by a factor of ∼3 as we move towards the NE tidal tail. Despite the drop, the cold gas dominates the flux (mass) budget across the targeted field of view, which might be fuelling the central starburst (visible in the optical wavelengths) as well as the putative AGN. The spatially resolved dominance of cold molecular gas is also consistent with the integrated spectral measurements discussed earlier in this section.

5 DISCUSSION

ULIRGs such as IR20551 provide ideal laboratories for studying the effects of feedback from starbursts and/or AGN on the host galaxy environment. The classification of IR20551 as AGN or starburst-dominated system depended on the wavelength band of observation. X-ray observations yield mixed results: *Chandra* detected the source (A. Ptak et al. 2003), *XMM–Newton* identified the source as hosting an obscured AGN (A. Franceschini et al. 2003), and NuSTAR detected only a marginal (2σ) signal in the 8–24 keV band (see S. Yamada et al. 2021). Despite the weak NuSTAR detection, the high column density reported in this system supports the presence of an obscured AGN (A. Franceschini et al. 2003). In contrast, optical spectroscopy previously classified IR20551 as an H II region (star-forming) galaxy (e.g. L. J. Kewley et al. 2001a). Our spatially resolved MUSE data enable the construction of a BPT map, which confirms H II-like ionization close to the central region of IR20551 in optical wavelengths (Fig. 10). The galaxy hosts two star-forming clumps, visible as the blue regions in the left panel of Fig. 10. However, the remainder of the field of view exhibits composite ionization, and in some off-nuclear regions even AGN-like signatures – although the line ratios observed in the [N II]and [O I] BPT diagrams show that the emission could also be associated with LINER emission from ISM shocks in a wind due to IR20551 being a late-stage merger.

The AGN nature of the nucleus cannot be ruled out based on diagnostic plots at mid-infrared wavelengths. While this source was previously classified as a starburst in the mid-infrared (e.g. R. Genzel et al. 1998), the mid-infrared spectral diagnostics ([Ne V]/[Ne II] versus PAH 6.2 μm EW) and colour–colour diagnostics ($F1500W/F560W$ versus $F770W/F560W$) based on synthetic photometry extracted from the MRS spectra place IR20551 at the boundary of the AGN-dominated and star-forming regimes (see Fig. 11). The MIRI imaging could not be used directly for this diagnostic as it is saturated in the centre. High-ionization emission lines such as [Ne V], which are characteristic tracers of AGN activity, are either weak or absent in the MRS spectra. Their absence may instead reflect the heavy obscuration in this system, as indicated also by the prominent 9.7 μm silicate absorption feature. Overall, based on mid-infrared diagnostics, the observations do not rule out the presence of an obscured AGN in IR20551, along with at least two central star-forming clumps, showing that the galaxy is also actively forming stars.

We investigated whether the AGN in IR20551 has a potential for any feedback on its host galaxy through outflows. Such outflows can, in principle, deplete the gas reservoir available for star formation and eventually quench star formation over long timescales. To test this, we examined the emission-line profiles of the ionized, warm, and cold molecular gas using MUSE, MRS, and ALMA spectra, respectively, searching for asymmetric or broad features. The integrated (aperture radius = 1.5 arcsec) normalized spectra of [O III], S(2), and CO(2–1), plotted on the same velocity scale in Fig. 12, reveal that the warm ionized gas traced by [O III] shows the broadest profile, with $w_{80} \sim 790$ km s^{-1}. The turbulent nature of the ionized gas is also visible in the v_{50} and w_{80} maps of [O III] presented in Fig. 9, which shows non-ordered motions. In contrast, the integrated CO(2–1) profile, although

Downloaded from https://academic.oup.com/mnras/article/549/1/stag781/8664325 by Instituto de Astrofisica de Canarias user on 26 June 2026

asymmetric and requiring two Gaussian components to reproduce, has a significantly narrower width of $w_{80} \sim 210$ km s^{-1}. The CO v_{50} maps at least show a relatively smooth gradient in the spatial profile compared to [O III]. This may suggest that the cold molecular gas moves more slowly than the ionized phase, possibly tracing the disc that is in the process of settling, and the observed asymmetries may simply reflect turbulent motions in the central regions, while the ionized gas is tracing the narrow-line region. The S(2) warm H_2 transition shows a width comparable to CO(2–1) but no evidence of asymmetric wings. While the absence of wings in the warm H_2 line could be partly due to the coarser spectral sampling of the MRS data, the current observations clearly suggest that neither molecular gas phase exhibits high-velocity outflows.

The absence of molecular gas outflows in IR20551 contrasts with numerous studies of AGN host galaxies, ULIRGs, and starbursts using *Spitzer*/IRS and *JWST*/MRS, where warm molecular outflows with velocity dispersions exceeding 400 km s^{-1} have been reported (e.g. K. M. Dasyra & F. Combes 2011; T. Bohn et al. 2024; J. H. Costa-Souza et al. 2024; K. Y. Dan et al. 2025; M. V. Zanchettin et al. 2025). However, the detection of outflows in a given gas phase strongly depends on factors such as the timescale of AGN-driven feedback, the efficiency of its coupling to the ISM, and the prevailing ISM conditions (see also C. M. Harrison & C. Ramos Almeida 2024). Physically, [O III]-based ionized gas originates mainly in the extended NLR, outside the galactic disc, making high-velocity outflows more readily detectable in this phase. By contrast, molecular gas resides predominantly in the disc, where any outflows are expected to be slower or their wings obscured by dust. Indeed, the H_2 line-width maps reveal turbulence within the central 5×5 arcsec^2 region, but the resolved widths remain around $\sim$200 km s^{-1}, which do not suggest a fast outflow in the molecular gas phases.

The excitation mechanism of the warm H_2 transitions is challenging to pin down, as they may arise from a variety of processes including shocks, radio jets, or external UV radiation. The excitation temperature maps in Fig. 13 show a peak near the putative AGN location, suggesting that UV radiation from the accretion disc likely dominates the heating of warm H_2 in the central region. A similar conclusion was reached for the nearby LIRG NGC 3256, based on H_2 line ratios (T. Bohn et al. 2024). As mentioned earlier, IR20551 also exhibits ionized gas outflows, pointing to the possible contribution of shocks in exciting H_2. Indeed, the models of L. E. Kristensen et al. (2023) suggest that the observed H_2 fluxes in IR20551, at least in the regions away from the AGN, can be explained with shock excitation. Radio jets have also been proposed as a mechanism for H_2 excitation (e.g. R. Davies et al. 2024), although the available radio data are at much lower spatial resolution than the MRS and ALMA data (see J. J. Condon et al. 2021). Based on the data presented here, the putative AGN likely plays a key role in powering the excitation of the warm H_2 transitions.

Finally, star formation in galaxies predominantly occurs in regions rich in cold molecular gas, and feedback from stars and/or AGN can act in either an ejective or preventative mode i.e. removing gas from the host galaxy or suppressing the ability of the available gas to form stars. In IR20551, we find fast ionized outflows but no evidence of an outflow in molecular gas phase or that the molecular gas is ejected. The warm molecular gas contributes <5 per cent of the total molecular reservoir. The warm gas is likely excited by AGN radiation and therefore has the potential to play a role in preventative feedback over longer time-scales. However,

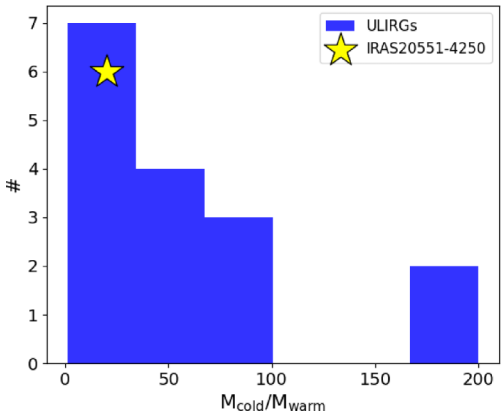


Figure 15. Distribution of cold-to-warm gas ratio in low-redshift ULIRGs from the literature. Warm gas masses in this distribution were obtained from the sample in A. O. Petric et al. (2018) and cold molecular gas masses from K. Alatalo et al. (2024). The observed cold molecular gas fraction of IR20551 is consistent with the range observed for low-redshift ULIRGs.

the cold molecular phase still remains dominant in IR20551. Similar cold-to-warm molecular gas fractions have been reported in outflows by T. Bohn et al. (2024). We compiled cold and warm molecular gas masses for a sample of low-redshift ULIRGs and derived their cold-to-warm molecular gas fractions, as shown in Fig. 15. The warm molecular gas masses presented in Fig. 15 are taken from A. O. Petric et al. (2018), based on a sub-sample of the parent GOALS galaxies from where IR20551 was selected. In A. O. Petric et al. (2018), warm gas masses are derived from integrated measurements of high-resolution *Spitzer*/IRS spectra, using the same methodology adopted in this paper. The cold molecular gas masses are drawn from integrated CARMA CO(1–0) observations of K. Alatalo et al. (2024), who assume an α_{CO} value of 1.5, comparable to the value of 1.8 used in this paper for IR20551. We find that the cold-to-warm molecular gas ratio in IR20551 is broadly consistent with those reported in the literature for low-redshift ULIRGs. However, we note that the cold gas mass estimate is subject to systematic uncertainties from assumed α_{CO} value, which relies on the physical conditions of the ISM such as shocks, photodissociated regions, metallicity, etc. (see D. Narayanan et al. 2012; A. D. Bolatto et al. 2013). Furthermore, these conditions change spatially depending on the local ISM conditions. Therefore, the flux ratio map between CO(2-1) and S(2) shown in Fig. 14 is under the assumption of a uniform α_{CO} value applied across the field of view.

In IR20551, the abundance of cold molecular gas reservoir ($M_{H_2}^{cold} \sim 1.3 \times 10^{10}$ M$_\odot$) suggests that star formation can continue largely unaffected, and feedback from the central source has not yet significantly altered the star-forming cycle. Although IR20551 hosts an ionized outflow, a mass outflow rate of <0.01 M$_\odot$ yr^{-1} in the centre does not appear sufficient to expel the molecular gas or suppress star formation on short time-scales. We also do not see any evidence of enhancement of star formation due to outflows or turbulent motions (e.g. G. Cresci et al. 2015a; P. S. Bessiere & C. Ramos Almeida 2022; J. Mercedes-Feliz et al. 2024). The Hα clump towards the SE of the putative AGN (Figs 8 and A3) happens to be at a location where the warm and cold molecular gas split into the tidal tails. However, this is outside the field of view of MRS observations and we cannot conclude

Downloaded from https://academic.oup.com/mnras/article/549/1/stag781/8664325 by Instituto de Astrofisica de Canarias user on 26 June 2026

whether this star-forming clump is indeed triggered due to warm or cold gas flows.

We note that additional phases, such as hot molecular gas traced by ro-vibrational transitions in the near-infrared ($T >$ 1000 K), also contribute to the molecular reservoir. However, this component generally represents only a small fraction compared to the warm and cold phases (e.g. D. Kakkad et al. 2025; M. V. Zanchettin et al. 2025). Thus, excluding the hot molecular gas from our analysis is unlikely to significantly impact the results presented in this paper.

6 SUMMARY AND FUTURE OUTLOOK

In this paper, we presented multiwavelength spatially resolved observations of IRAS20551-4250, a ULIRG at redshift $z = 0.0429$, using imaging and spectroscopy from *JWST* (MIRI, MRS, and NIRCam), *HST* (ACS), VLT (MUSE), and ALMA. Our goal was to characterize the warm and cold molecular gas within the central 5×5 arcsec^2 ($\sim 4 \times 4$ kpc^2) of the galaxy and assess the impact of the AGN on the multiphase molecular gas properties. To this end, we first examined whether AGN ionization dominates at the observed wavelengths, followed by a detailed characterization of the warm molecular gas traced using the rotational transitions in the mid-infrared spectra (temperature, mass, distribution, kinematics), which we then compared with the cold gas properties derived from ALMA observations. Here, we summarize the main findings of this paper:

(i) The wide field images of IRAS20551-4250 show tidal tails. At optical wavelengths, the central region of the galaxy shows a disturbed morphology, but as we move to the near-infrared and mid-infrared wavelengths, a central bright source becomes prominent. Spectral and colour–colour diagnostics in the mid-infrared wavelengths does not rule out the AGN nature of the central source. The MRS spectra show a deep silicate feature that suggests a possible presence of an obscured AGN. The galaxy also hosts a starburst, confirmed via BPT diagrams constructed using optical IFU observations from MUSE, confirming the composite nature of the source as reported in previous literature.

(ii) We detect several rotational H_2 transitions in the MRS spectra, from S(1) to S(8). The excitation diagram of these transitions suggest that the molecular gas can be approximately grouped into two temperatures: one warm molecular gas at $\sim$500 K and other hot gas at $\sim$1400 K. The excitation map suggests that the putative AGN may be the likely source for exciting the rotational transitions, but the observed warm gas fluxes could also be explained using shocks.

(iii) Fast outflows with velocity dispersion $\sim$790 km s^{-1} and mass outflow rate of < 0.01 M$_\odot$ yr^{-1} are observed in the [O III]5007-based ionized gas phase, while the cold and warm molecular gas, with velocity dispersions $\sim$200 km s^{-1}, show slow moving or no outflows.

(iv) The warm and cold molecular gas are co-located and show similar kinematics. Both gas phases show two tidal tails and the central region of this galaxy appears to be in the process of settling into a rotating disc.

(v) We find a warm molecular gas mass of 6.1×10^8 M$_\odot$ and cold molecular gas of 1.3×10^{10} M$_\odot$, i.e. warm molecular gas constitutes <5 per cent of the total molecular gas in this galaxy. The cold-to-warm molecular gas fraction is consistent with literature measurements of low-redshift ULIRGs. The higher amount of cold molecular gas suggests that the galaxy still has sufficient amount of cold molecular gas to continue forming stars in the centre. The ionized gas mass outflow rate of < 0.01 M$_\odot$ yr^{-1} appear insufficient to immediately disrupt the star-forming ability of IR20551.

IRAS20551-4250, with its observed cold-to-warm molecular gas ratios, ongoing star formation, and the presence of ionized outflows, represents a ULIRG that hosts an ionized outflow, indicated by high [O III]velocity dispersion values, but the outflow is not sufficient to develop the wide-scale feedback needed to impact the galaxy's star-forming capacity. Expanding such analyses with *JWST*/MRS and ALMA observations of a larger sample of low-redshift ULIRGs and AGN hosts will provide the means to assess more generally whether observations of outflows and subsequent feedback from the AGN are a common occurence or do we expect to see more galaxies like IRAS20551-4250 where the AGN appears to have minimal impact on the star formation cycle.

ACKNOWLEDGEMENTS

We thank the anonymous referee for their constructive comments and suggestions. CR acknowledges support from SNSF Consolidator grant F01-13252, Fondecyt Regular grant 1230345, ANID BASAL project FB210003 and the China-Chile joint research fund. VU acknowledges funding support from NSF Astronomy and Astrophysics Grant (AAG) No. AST-2536603, NASA Astrophysics Data Analysis Program (ADAP) grant No. 80NSSC23K0750, NASA Astrophysics Decadal Survey Precursor Science (ADSPS) grant No. 80NSSC25K0169, and STScI grant Nos. HST-GO-17285.001-A and JWST-GO-01717.001-A. MSG acknowledges support by the Hellenic Foundation for Research and Innovation (HFRI) under the '2nd Call for HFRI Research Projects to support Faculty Members & Researchers' (Project Number: 03382). This paper makes use of the following ALMA data: ADS/JAO.ALMA#2022.1.01262.S. ALMA is a partnership of ESO (representing its member states), NSF (USA), and NINS (Japan), together with NRC (Canada), NSC and ASIAA (Taiwan), and KASI (Republic of Korea), in cooperation with the Republic of Chile. The Joint ALMA Observatory is operated by ESO, AUI/NRAO, and NAOJ. This research is based on observations made with the NASA/ESA *Hubble Space Telescope* obtained from the Space Telescope Science Institute, which is operated by the Association of Universities for Research in Astronomy, Inc., under NASA contract NAS 5–26555. These observations are associated with program 10592. This work is based [in part] on observations made with the NASA/ESA/CSA *James Webb Space Telescope*. The data were obtained from the Mikulski Archive for Space Telescopes at the Space Telescope Science Institute, which is operated by the Association of Universities for Research in Astronomy, Inc., under NASA contract NAS 5–03127 for *JWST*. These observations are associated with program 3368.

DATA AVAILABILITY

The data can be retrieved from MAST archive under the programme IDs 10592 (*HST*) and 3368 (*JWST*). ALMA data are available from the ALMA archive under the programme ID 2022.1.01262.S and the MUSE data are available under the programme ID 095.B-0049.

Downloaded from https://academic.oup.com/mnras/article/549/1/stag781/8664325 by Instituto de Astrofisica de Canarias user on 26 June 2026

REFERENCES

Alatalo K. et al., 2024, ApJ, 975, 241
Armus L. et al., 2007, ApJ, 656, 148
Armus L. et al., 2009, PASP, 121, 559
Armus L. et al., 2023, ApJ, 942, L37
Baldwin J. A., Phillips M. M., Terlevich R., 1981, PASP, 93, 5
Bernard-Salas J. et al., 2009, ApJS, 184, 230
Bertola E. et al., 2024, A&A, 691, 178
Bessiere P. S., Ramos Almeida C., 2022, MNRAS, 512, L54
Bianchin M. et al., 2024, ApJ, 965, 103
Bohn T. et al., 2024, ApJ, 977, 36
Bolatto A. D., Wolfire M., Leroy A. K., 2013, ARA&A, 51, 207
Briggs D. S., 1995, PhD thesis, New Mexico Institute of Mining and Technology
Burton M. G., Hollenbach D. J., Tielens A. G. G., 1992, ApJ, 399, 563
CASA Team, 2022, PASP, 134, 114501
Cappellari M., 2017, MNRAS, 466, 798
Cappellari M., Emsellem E., 2004, PASP, 116, 138
Carilli C. L., Walter F., 2013, ARA&A, 51, 105
Carniani S. et al., 2016, A&A, 591, A28
Castro A. et al., 2025, New Astron., 121, 102433
Cicone C. et al., 2014, A&A, 562, A21
Circosta C. et al., 2021, A&A, 646, A96
Condon J. J., Cotton W. D., Jarrett T., Marchetti L., Matthews A. M., Mauch T., Moloko M. E., 2021, ApJS, 257, 35
Cornwell T. J., 2008, IEEE J. Sel. Top. Signal Process., 2, 793
Costa-Souza J. H., Riffel R. A., Souza-Oliveira G. L., Zakamska N. L., Bianchin M., Storchi-Bergmann T., Riffel R., 2024, ApJ, 974, 127
Cresci G. et al., 2015a, A&A, 582, A63
Cresci G. et al., 2015b, ApJ, 799, 82
Dan K. Y. et al., 2025, ApJ, 979, 68
Dasyra K. M., Combes F., 2011, A&A, 533, L10
Dasyra K. M. et al., 2024, ApJ, 977, 156
Davies R. et al., 2020, MNRAS, 498, 4150
Davies R. et al., 2024, A&A, 689, A263
Diaz-Santos T. et al., 2025, Astrophysics Source Code Library, record ascl:2501.001
Esparza-Arredondo D. et al., 2025, A&A, 693, A174
Evans A. S. et al., 2022, ApJ, 940, L8
Farrah D. et al., 2007, ApJ, 667, 149
Feruglio C., Fabbiano G., Bischetti M., Elvis M., Travascio A., Fiore F., 2020, ApJ, 890, 29
Franceschini A. et al., 2003, MNRAS, 343, 1181
Furton D. G., Laiho J. W., Witt A. N., 1999, ApJ, 526, 752
García-Burillo S. et al., 2021, A&A, 652, A98
Genzel R. et al., 1998, ApJ, 498, 579
Genzel R. et al., 2014, ApJ, 796, 7
Haan S. et al., 2011, AJ, 141, 100
Harrison C. M., Ramos Almeida C., 2024, Galaxies, 12, 17
Harrison C. M., Alexander D. M., Mullaney J. R., Swinbank A. M., 2014, MNRAS, 441, 3306
Herrero-Illana R. et al., 2019, A&A, 628, A71
Hickox R. C., Alexander D. M., 2018, ARA&A, 56, 625
Higdon S. J. U., Armus L., Higdon J. L., Soifer B. T., Spoon H. W. W., 2006, ApJ, 648, 323
Ho I. T. et al., 2016, Ap&SS, 361, 280
Högbom J. A., 1974, A&AS, 15, 417
Hopkins P. F. et al., 2018, MNRAS, 480, 800
Husemann B., Davis T. A., Jahnke K., Dannerbauer H., Urrutia T., Hodge J., 2017, MNRAS, 470, 1570
Imanishi M., Nakanishi K., Izumi T., 2016, ApJ, 825, 44
Inami H. et al., 2022, ApJ, 940, L6
Iono D. et al., 2009, ApJ, 695, 1537
Johansson L., 1991, A&A, 241, 389
Kakkad D. et al., 2017, MNRAS, 468, 4205
Kakkad D. et al., 2020, A&A, 642, A147
Kakkad D. et al., 2022, MNRAS, 511, 2105
Kakkad D., Stalevski M., Kishimoto M., Knežević S., Asmus D., Vogt F. P. A., 2023, MNRAS, 519, 5324
Kakkad D. et al., 2025, MNRAS, 541, 3534
Kauffmann G. et al., 2003, MNRAS, 346, 1055
Kennicutt R. C., Evans N. J., 2012, ARA&A, 50, 531
Kepley A. A., Tsutsumi T., Brogan C. L., Indebetouw R., Yoon I., Mason B., Donovan Meyer J., 2020, PASP, 132, 024505
Kewley L. J., Heisler C. A., Dopita M. A., Lumsden S., 2001a, ApJS, 132, 37
Kewley L. J., Dopita M. A., Sutherland R. S., Heisler C. A., Trevena J., 2001b, ApJ, 556, 121
Kewley L. J., Dopita M. A., Leitherer C., Davé R., Yuan T., Allen M., Groves B., Sutherland R., 2013, ApJ, 774, 100
Koss M. J. et al., 2021, ApJS, 252, 29
Koudmani S., Sijacki D., Smith M. C., 2022, MNRAS, 516, 2112
Kreckel K. et al., 2018, ApJ, 863, L21
Kristensen L. E., Godard B., Guillard P., Gusdorf A., Pineau des Forêts G., 2023, A&A, 675, A86
Labiano A. et al., 2016, in Peck A. B., Seaman R. L., Benn C. R., eds, Proc. SPIE Conf. Ser. Vol. 9910, Observatory Operations: Strategies, Processes, and Systems VI. SPIE, Bellingham, p. 99102W
Lai T. S. Y. et al., 2022, ApJ, 941, L36
Lamperti I. et al., 2022, A&A, 668, A45
Law D. R., E. Morrison J., Argyriou I., Patapis P., Álvarez-Márquez J., Labiano A., Vandenbussche B., 2023, AJ, 166, 45
Leroy A. K. et al., 2021, ApJS, 255, 19
Maiolino R. et al., 2017, Nature, 544, 202
Malkan M. A., Jensen L. D., Hao L., 2026, ApJ, 998, 165
Maloney P., Black J. H., 1988, ApJ, 325, 389
Marshall J. A., Herter T. L., Armus L., Charmandaris V., Spoon H. W. W., Bernard-Salas J., Houck J. R., 2007, ApJ, 670, 129
Mercedes-Feliz J. et al., 2024, MNRAS, 530, 2795
Misaki K., Iwasawa K., Taniguchi Y., Terashima Y., Kunieda H., Watarai H., 1999, Adv. Space Res., 23, 1051
Narayanan D., Krumholz M. R., Ostriker E. C., Hernquist L., 2012, MNRAS, 421, 3127
Padovani P. et al., 2017, A&AR, 25, 2
Papadopoulos P. P., van der Werf P. P., Xilouris E. M., Isaak K. G., Gao Y., Mühle S., 2012, MNRAS, 426, 2601
Pereira-Santaella M. et al., 2018, A&A, 616, A171
Petric A. O. et al., 2018, AJ, 156, 295
Pillepich A. et al., 2018, MNRAS, 473, 4077
Piotrowska J. M., Bluck A. F. L., Maiolino R., Peng Y., 2022, MNRAS, 512, 1052
Ptak A., Heckman T., Levenson N. A., Weaver K., Strickland D., 2003, ApJ, 592, 782
Rieke G. H. et al., 2025, ApJ, 988, 17
Riffel R. A. et al., 2023, MNRAS, 521, 1832
Rigopoulou D., Kunze D., Lutz D., Genzel R., Moorwood A. F. M., 2002, A&A, 389, 374
Robbins S. L., Raimundo S. I., Malkan M. A., 2025, ApJ, 980, 64
Rosario D. J. et al., 2018, MNRAS, 473, 5658
Rosario D. J., Togi A., Burtscher L., Davies R. I., Shimizu T. T., Lutz D., 2019, ApJ, 875, L8
Rupke D. S. N., Veilleux S., 2011, ApJ, 729, L27
Saade M. L., Brightman M., Stern D., Malkan M. A., García J. A., 2022, ApJ, 936, 162
Saintonge A., Catinella B., 2022, ARA&A, 60, 319
Sanders D. B., Mazzarella J. M., Kim D. C., Surace J. A., Soifer B. T., 2003, AJ, 126, 1607
Sani E., Nardini E., 2012, Adv. Astron., 2012, 783451
Schawinski K., Koss M., Berney S., Sartori L. F., 2015, MNRAS, 451, 2517
Schaye J. et al., 2015, MNRAS, 446, 521
Schaye J. et al., 2023, MNRAS, 526, 4978
Scholtz J. et al., 2020, MNRAS, 492, 3194
Schwarz G., 1978, Ann. Stat., 6, 461
Solomon P. M., Vanden Bout P. A., 2005, ARA&A, 43, 677

Downloaded from https://academic.oup.com/mnras/article/549/1/stag781/8664325 by Instituto de Astrofisica de Canarias user on 26 June 2026

Spinoglio L., Fernández-Ontiveros J. A., Malkan M. A., 2022, ApJ, 941, 46
Spoon H. W. W., Marshall J. A., Houck J. R., Elitzur M., Hao L., Armus L., Brandl B. R., Charmandaris V., 2007, ApJ, 654, L49
Stierwalt S. et al., 2013, ApJS, 206, 1
Stierwalt S. et al., 2014, ApJ, 790, 124
Sugai H., Malkan M. A., 2000, ApJ, 529, 219
Sugai H., Malkan M. A., Ward M. J., Davies R. I., McLean I. S., 1997, ApJ, 481, 186
Togi A., Smith J. D. T., 2016, ApJ, 830, 18
Tommasin S., Spinoglio L., Malkan M. A., Fazio G., 2010, ApJ, 709, 1257
U V. et al., 2019, ApJ, 871, 166
Vayner A. et al., 2024, ApJ, 960, 126
Veilleux S., Osterbrock D. E., 1987, ApJS, 63, 295
Veilleux S., Maiolino R., Bolatto A. D., Aalto S., 2020, A&A Rev., 28, 2
Vogelsberger M., Marinacci F., Torrey P., Puchwein E., 2020, Nat. Rev. Phys., 2, 42
Weldon A. et al., 2024, MNRAS, 531, 4560
Wells M. et al., 2015, PASP, 127, 646
West R. M., Borchkhadze T. M., Breysacher J., Laustsen S., Schuster H. E., 1978, A&AS, 31, 55
Wu Y., Charmandaris V., Huang J., Spinoglio L., Tommasin S., 2009, ApJ, 701, 658
Wylezalek D., Flores A. M., Zakamska N. L., Greene J. E., Riffel R. A., 2020, MNRAS, 492, 4680
Yamada S., Ueda Y., Tanimoto A., Imanishi M., Toba Y., Ricci C., Privon G. C., 2021, ApJS, 257, 61
Zakamska N. L., 2010, Nature, 465, 60
Zanchettin M. V., Ramos Almeida C., Audibert A., Acosta-Pulido J. A., Cezar P. H., Hicks E., Lapi A., Mullaney J., 2025, A&A, 695, A185

APPENDIX A: APPENDIX

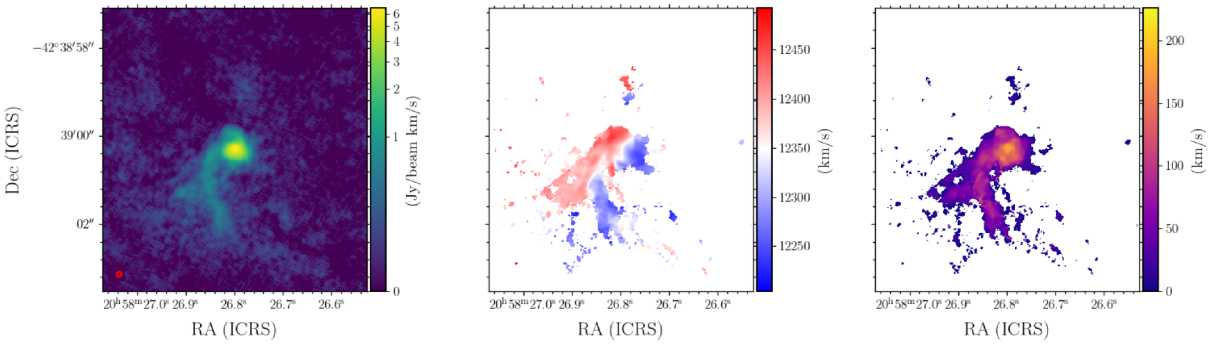


Figure A1. Native resolution ALMA CO(2-1) maps of IR20551: Moment 0 (left panel), Moment 1 (middle panel), and Moment 2 (right panel).

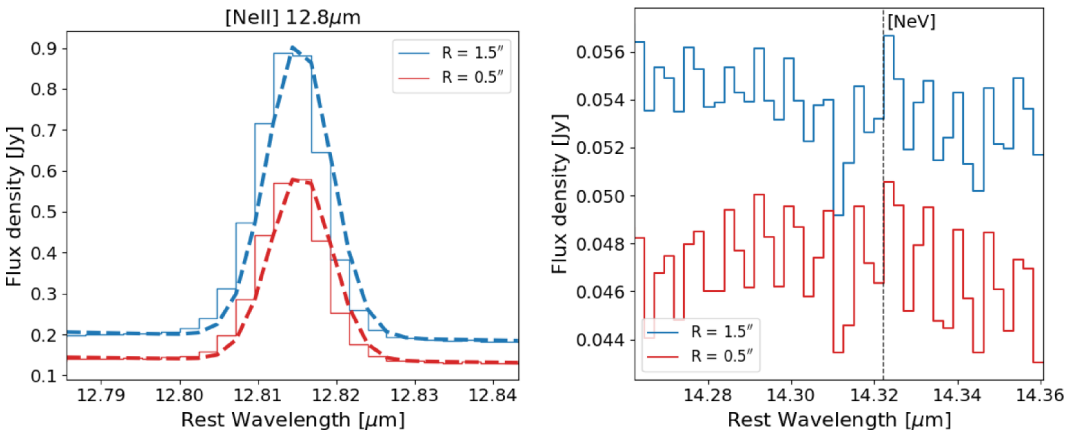


Figure A2. [Ne II]12.8 (left) and [Ne V]14.3 (right) emission in the nuclear and integrated MRS apertures of IR20551. [Ne V] emission is absent or weak, the latter indicated by a small positive flux near its expected location.

Downloaded from https://academic.oup.com/mnras/article/549/1/stag781/8664325 by Instituto de Astrofisica de Canarias user on 26 June 2026

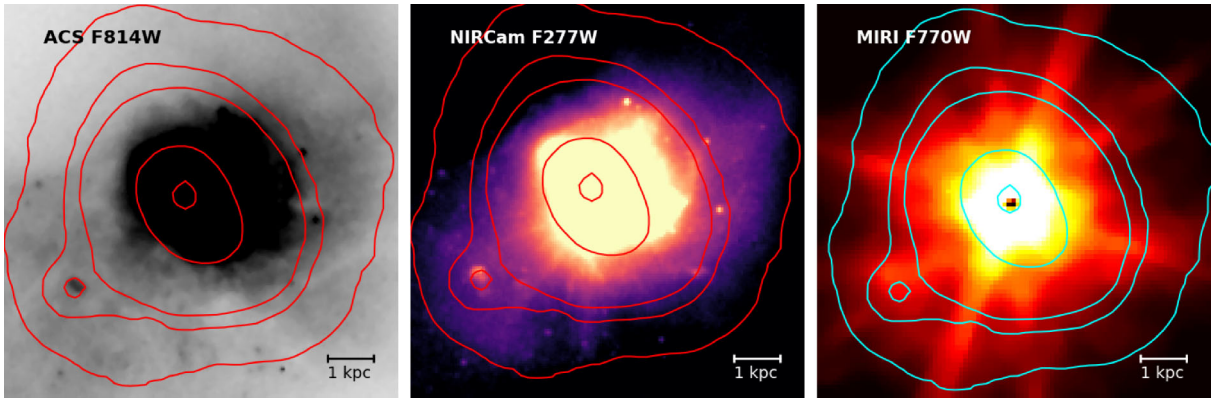


Figure A3. *HST* ACS/F814W (left), *JWST* NIRCam/*F277W* (middle) and *JWST* MIRI/*F770W* (right) images with H α contours from Fig. 8 overlaid in red and cyan at levels 2 per cent, 5 per cent, 10 per cent, 40 per cent, and 95 per cent of the peak H α flux. The contours levels are chosen to visually guide the structures in the H α map. The second H α clump towards the SE of the central source clearly coincides with peaks in the *F*814*W* and *F*277*W* images.

[1]*Centre for Astrophysics Research, Department of Physics, Astronomy and Mathematics, University of Hertfordshire, Hatfield AL10 9AB, UK*
[2]*Space Telescope Science Institute, 3700 San Martin Drive, Baltimore, MD 21210, USA*
[3]*European Southern Observatory, Alonso de Córdova, 3107, Vitacura, Santiago 763-0355, Chile*
[4]*Joint ALMA Observatory, Alonso de Córdova, 3107, Vitacura, Santiago 763-0355, Chile*
[5]*IPAC, California Institute of Technology, 1200 East California Boulevard, Pasadena, CA 91125, USA*
[6]*Department of Physics and Astronomy, UCLA, Los Angeles, CA 90095, USA*
[7]*AURA for the European Space Agency (ESA), Space Telescope Science Institute, 3700 San Martin Drive, Baltimore, MD 21218, USA*
[8]*Department of Astronomy, University of Virginia, 530 McCormick Road, Charlottesville, VA 22903, USA*
[9]*National Radio Astronomy Observatory, 520 Edgemont Road, Charlottesville, VA 22903, USA*
[10]*Caltech/IPAC, MC 314-6, 1200 E. California Blvd., Pasadena, CA 91125, USA*
[11]*Department of Physics and Astronomy, 4129 Frederick Reines Hall, University of California, Irvine, CA 92697, USA*
[12]*Instituto de Astrofisica de Canarias, Calle Via Láctea, s/n, E-38205, La Laguna, Tenerife, Spain*
[13]*Departamento de Astrofisica, Universidad de La Laguna, E-38206, La Laguna, Tenerife, Spain*
[14]*European Space Agency, Space Telescope Science Institute, Baltimore, MD 21218, USA*
[15]*Ehime University, Bunkyo-cho 2-5, Matsuyama, Ehime 790-8577, Japan*
[16]*Leiden Observatory, Leiden University, PO Box 9513, NL-2300 RA Leiden, the Netherlands*
[17]*School of Sciences, European University Cyprus, Diogenes Street, Engomi, Nicosia 1516, Cyprus*
[18]*Institute of Astrophysics, Foundation for Research and Technology-Hellas (FORTH), Heraklion 70013, Greece*
[19]*Department of Physics, University of Crete, Heraklion 71003, Greece*
[20]*Hiroshima Astrophysical Science Center, Hiroshima University, 1-3-1 Kagamiyama, Higashi-Hiroshima, Hiroshima 739-8526, Japan*
[21]*Steward Observatory, University of Arizona, 933 North Cherry Avenue, Tucson, AZ 85721, USA*
[22]*Dipartimento di Fisica e Astronomia, Università di Padova, Vicolo dell'Osservatorio 3, I-35122 Padova, Italy*
[23]*Department of Astronomy, University of Florida, P.O. Box 112055, Gainesville, FL 32611, USA*
[24]*Department of Astronomy, University of Geneva, ch. d'Ecogia 16, SE-1290 Versoix, Switzerland*
[25]*Instituto de Estudios Astrofisicos, Facultad de Ingeniería y Ciencias, Universidad Diego Portales, Av. Ejército Libertador 441, Santiago, Chile*
[26]*Institute for Astronomy, University of Hawaii, 2680 Woodlawn Drive, Honolulu, HI 96822, USA*
[27]*Department of Astronomy, University of Virginia, P.O. Box 400325, Charlottesville, VA 22904, USA*

This paper has been typeset from a TEX/LATEX file prepared by the author.

Downloaded from https://academic.oup.com/mnras/article/549/1/stag781/8664325 by Instituto de Astrofisica de Canarias user on 26 June 2026

© The Author(s) 2026.
Published by Oxford University Press on behalf of Royal Astronomical Society. This is an Open Access article distributed under the terms of the Creative Commons Attribution License (https://creativecommons.org/licenses/by/4.0/), which permits unrestricted reuse, distribution, and reproduction in any medium, provided the original work is properly cited.